JOURNAL OF CARDIOVASCULAR MAGNETIC RESONANCE®
Vol. 6, No. 1, pp. 103–126, 2004

Moderated Poster Presentations

201. A Combined Single-Session Analysis of Adenosine Perfusion and of High-Dose Dobutamine Stress Cardiovascular Magnetic Resonance Improves Diagnosis of Ischemia

Andreas Wahl, MD,[1] Ingo Paetsch, MD,[2] Stefan Roethemeyer, MD,[2] Rolf Gebker, MD,[2] Christoph Klein, MD,[2] Eckart Fleck, MD,[2] Eike Nagel, MD[2].
[1]*Cardiology, Swiss Cardiovascular Center Bern, Bern, Switzerland,*[2]*Cardiology, German Heart Institute Berlin, Berlin, Germany.*

Introduction: With CMR, both the analysis of myocardial perfusion during adenosine stress (Perfusion-CMR) and of wall motion during dobutamine stress (Stress-CMR) were shown highly accurate for the diagnosis of myocardial ischemia. A combined single session dual stress protocol has not been reported so far.

Purpose: To compare the diagnostic accuracy of perfusion-CMR and stress-CMR in an unselected patient population, and to determine whether a combined single-session assessment of myocardial perfusion and wall motion improves diagnosis of ischemia, with invasive quantitative coronary angiography serving as reference standard.

Methods: 100 consecutive patients with signs or symptoms of coronary artery disease (mean age 62±9 years; prior myocardial infarction: 30%; prior PTCA: 48% and CABG: 27%) were examined (1.5 T ACS NT Philips) prior to clinically indicated invasive coronary angiography. Myocardial perfusion was visually assessed during the first pass of a contrast agent bolus from 60 dynamics (3 short axis images acquired every heartbeat; TFE-EPI hybrid sequence; pp-delay 200 ms; TR/TE/flip 3.6/12/30) during adenosine infusion (140 $ug.kg^{-1}.min^{-1}$) and at rest. Stress-CMR images were acquired at rest and during a standardized high-dose dobutamine-atropine protocol in 3 short-axis (same 3 short-axis views as for perfusion-CMR), a 4-, a 3- and a 2-chamber view (single slice steady state free precession technique; TR/TE/flip 3.0/1.5/55). Regional wall motion was assessed using a multiple screen format, a 16 segment model, and a 4-point scoring system. A new or worsening wall motion abnormality in ≥ 1 segment was considered positive for ischemia. In the absence of ischemia, failure to attain 85% of age-predicted maximal heart rate was defined as a non-diagnostic result.

Results: Significant coronary artery disease ($\geq 50\%$ diameter stenoses by quantitative invasive coronary angiography) was found in 69% of patients. No significant adverse effects occurred during stress testing. Sensitivity, specificity and diagnostic accuracy of stress-CMR were 87%, 84% and 86%, respectively, with one non-diagnostic test (1%; target heart rate not

Table 1.

	Sensitivity	Specificity	Accuracy	% diagnostic examinations
Stress-CMR	87	84	86	99
Perfusion-CMR	88	77	85	97
Perfusion-CMR and Stress-CMR pathologic	77	90	81	96
Perfusion-CMR or Stress-CMR pathologic	97	71	89	100

DOI: 10.1081/JCMR-120028312
1097-6647 (Print); 1532-429X (Online)
Copyright © 2004 by Marcel Dekker, Inc.
www.dekker.com

ORDER REPRINTS

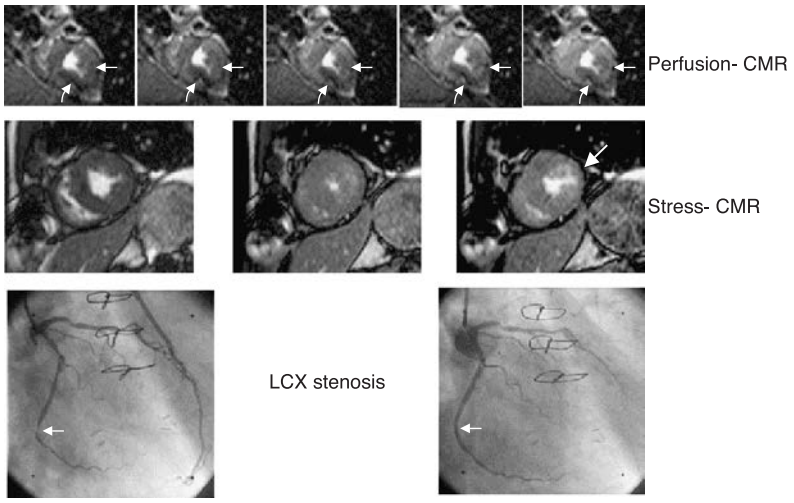

Figure 1.

reached). For perfusion-CMR, sensitivity, specificity and diagnostic accuracy were 88%, 77% and 85%, respectively, with 3 non-diagnostic tests (3%; poor image quality). For a combined approach, these values were 97%, 71% and 89%, respectively, with 100% diagnostic tests (Table 1, Fig. 1).

Conclusions: A combined single session assessment of perfusion-CMR and stress-CMR is safe and feasible. Visual assessment of perfusion-CMR has similar diagnostic accuracy than stress-CMR. A combined analysis only marginally improves diagnostic accuracy and marginally increases the number of diagnostic examinations.

202. Low Dose Dobutamine Stress MR Is Superior to Infarct Imaging for the Prediction of Functional Recovery After Revascularization

Eike Nagel, 1967, MD, Ernst Wellnhofer, Adriana Olariu, Christoph Klein, Michael Gräfe, Eckart Fleck. *Cardiology, German Heart Institute Berlin, Berlin, Germany.*

Introduction: Magnetic resonance imaging (MRI) with delayed enhancement(SCAR) predicts functional recovery after revascularization. Low-dose dobutamine tests have been used to diagnose viability for many years.

Purpose: To determine the diagnostic value of low dose dobutamine stress MR (DSMR) in comparison to SCAR fordetection of hibernating myocardium.

Methods: In 29 consecutive patients with coronary artery disease (68±7 yrs, 3 females, ejection fraction 35±7%), scheduled for revascularization, wall motion was evaluated semi-quantitatively (16 segments) by MRI (Philips ACS, NT, 1.5 Tesla) before and 3 months after intervention. Scar imaging (with Gd-DTPA, and low-dose DSMR were performed before revascularization. The transmural extent of scar was assessed semi-quantitatively (25% steps). The analysis was based on 195/288 revascularized segments with wall motion abnormalities at rest. Logistic regression was used for modeling of binary prediction. ROC-AUC statistics were used to compare different models.

Results: Low-dose DSMR (AUC=0.861) was superior to SCAR (AUC 0.763) for the prediction of functional recovery. Adding SCAR to DSMR did not improve accuracy of prediction. Subgroup analysis based on transmurality of scar showed superiority of DSMR for 1–74% tranmural extent of infarction (Fig. 1).

Conclusions: Low-dose DSMR is superior to scar imaging as predictor of functional recovery. This improvement is most pronounced in segments with delayed enhancement <75%.

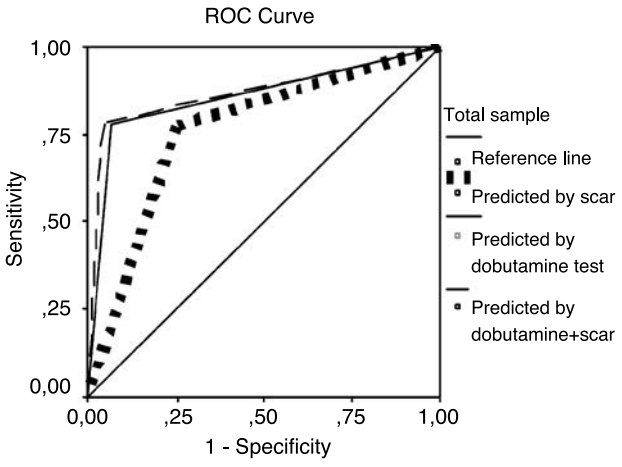

Figure 1.

Copyright © Marcel Dekker, Inc. All rights reserved.

ORDER REPRINTS

203. Age-Related Differences in Aortic Distensibility Modulate Left Ventricular Remodeling After Myocardial Infarction

Glenn A. Hirsch, M.D.,[1] W. P. Ingkanisorn, M.D.,[2] Christopher K. Dyke, M.D.,[2] Kenneth L. Rhoads, M.D.,[2] Steven P. Schulman, M.D.,[3] Gary Gerstenblith, M.D.,[3] Anthony H. Aletras, Ph.D.,[2] Andrew E. Arai, M.D.[2] [1]*Cardiology, Johns Hopkins/NHLBI, Bethesda, MD, USA,* [2]*Laboratory of Cardiac Energetics, NHLBI, Bethesda, MD, USA,* [3]*Cardiology, Johns Hopkins Hospital, Baltimore, MD, USA.*

Introduction: After myocardial infarction (MI), there in an exponential increase in mortality with increasing age from age 60 to greater than 85 years. Although the mechanism is unknown, age-related increases in vascular may contribute to adverse left ventricular (LV) remodeling after MI. Contrast-enhanced cardiac MR allows accurate quantification of LV volumes, MI size, and vascular stiffness (aortic distensibility). Therapies that decrease vascular stiffness may help decrease the high morbidity and mortality of older patients after MI.

Purpose: We used contrast-enhanced cardiac MRI to evaluate the hypothesis that age-related vascular stiffness modulates left ventricular remodeling after MI.

Methods: This was a cross-sectional study of 49 patients with a history of MI undergoing CMR. Measurements included LV end-systolic volume index (ESVI), end-diastolic volume index (EDVI), ejection fraction (EF), MI size, and aortic distensibilility. The cohort was stratified by age (less than or greater than 60) for analysis.

Univariate analyses of variables predictive of ESVI and a multivariate analysis for prediction of ESVI were also performed.

Results: The demographics of the two groups were similar except for more of the older patients taking an ACE inhibitor (83% vs. 47% respectively, $p<0.01$). Despite no difference in MI size between the older and younger groups respectively (37 ± 26 vs. 35 ± 27 grams, $p=0.79$), the older cohort had higher ESVI (78 ± 52 vs. 44 ± 17 mL/m^2, $p<0.01$), EDVI (123 ± 48 vs. 91 ± 22 mL/m^2, $p<0.01$), and overall lower average EF (41 ± 16 vs. $53\pm11\%$, $p<0.01$). Older patients had significantly higher end systolic volumes and lower EF for a given MI size than younger patients (ANCOVA, $p<0.0001$). Aortic distensibility was inversely correlated with age ($r=-0.75$, $p<0.0001$) and was significantly lower in patients ≥ 60 years compared to those under 60 years (9.1×10^{-4} vs. 1.1×10^{-3} mmHg^{-1}, $p<0.0001$).

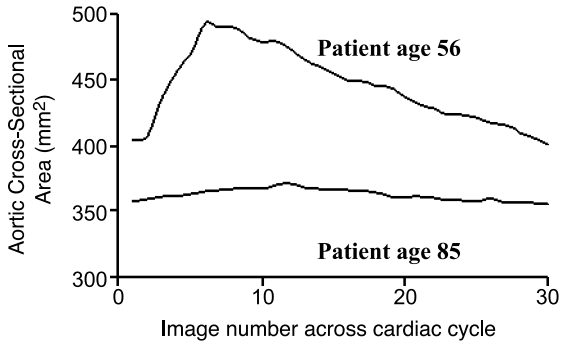

Figure 1. Aortic distensibility decreases with age.

Representative aortic distensibility curves are shown in Figure 1. Univariate analyses suggested age, aortic distensibility, and MI size as significant predictors of ESVI. Multivariate analysis demonstrated MI size ($p<0.001$) and aortic distensibility ($p=0.02$) as significant predictors of ESVI when adjusted for age.

Conclusions: Older patients experience increased remodeling after myocardial infarction compared to younger patients. Age-related decreases in aortic distensibility contribute to post-infarction LV remodeling.

204. High-Resolution Black-Blood MRI of Human Carotid Atherosclerotic Plaque: Comparison of Three- and Two-dimensional Methods

Vasily L. Yarnykh, PhD, Baocheng Chu, MD, PhD, Thomas S. Hatsukami, MD, Chun Yuan, PhD. *Radiology, University of Washington, Seattle, WA, USA.*

Introduction: Most current protocols for high-resolution imaging of carotid arteries (CA's) are based on 2D black-blood (BB) techniques (Fayad and Fuster, 2000; Yuan et al., 2001). An evident limitation of 2D imaging is a large slice thickness (2–3 mm) relative to the size of atherosclerotic plaque. Although 3D imaging may overcome this limitation, advantages and disadvantages of 3D BB carotid MRI were not systematically evaluated. Promising results were reported for coronary arteries (Stuber et al., 2001) using a 3D fast spin-echo (FSE) sequence with double inversion-recovery (DIR) preparation. Previous experience in 3D BB carotid MRI has been focused on a decrease of scan time by using sequences with reduced field-of-view (FOV) (Crowe et al., 2003; Luk-Pat et al., 1999), which cannot be used for routine bilateral

Copyright © Marcel Dekker, Inc. All rights reserved.

ORDER REPRINTS

Table 1. Scan parameters for 2D and 3D BB DIR-FSE sequences.

Parameter	2D DIR-FSE	3D DIR-FSE
TR/TE/TI, ms	800/11/330	600/27/260
Echo train	8	8
In-plane resolution, mm	0.63 (0.31)[a]	0.63 (0.31)[a]
Slice thickness, mm	2	1 (0.5)[a]
Number of slices	10	20 (40)[a]
NEX	2	1
Scan time, min	6.5	6

[a]After zero-interpolation.

examinations. While long scan time is a general problem of the 3D FSE technique, T_1-weighted (T1W) imaging with short TR may benefit from 3D acquisition due to increased SNR and improved slice resolution without time penalties.

Purpose: To develop and optimize a 3D DIR-FSE sequence for routine T1W imaging of carotid arteries and to compare it with a 2D method.

Methods: The 2D and 3D BB sequences were implemented with FSE readout and DIR preparation. Images were obtained on a 1.5T MR scanner (GE Signa Echospeed) using a four-element phased-array coil. Scan parameters are listed in Table 1. The group of subjects included five healthy volunteers and nine patients with carotid atherosclerosis. To determine an influence of slab thickness on flow suppression in the 3D method, in two volunteers 3D images were acquired with the slice thickness of 2 mm while varying the number of slices in a range of 8–32. For other subjects, parameters of 2D and 3D sequences were chosen to provide identical spatial coverage and close scan time (Table 1). The quality of flow suppression was estimated by signal-to-noise ratios (SNR's) in the lumina of CA's and jugular veins (JV's). Image SNR's were compared in the matched regions of interest placed into sternocleidomastoid (SCM) muscles.

Results: Results of image analysis are listed in Table 2. 3D T1W imaging with a single acquisition (NEX=1) provided the same or better SNR (depending on slice thickness) as in the 2D protocol with two acquisitions (NEX=2). This advantage allowed double improvement in slice resolution. Axial 2D and 3D images demonstrated similar quality and appearance of

Table 2. Image quality characteristics for 2D and 3D scans.

Parameter	2D DIR-FSE	3D DIR-FSE
SNR in CA's	1.1±0.10	1.4±0.4
SNR in JV's	1.1±0.10	1.6±0.3
SNR in SCM muscle	11.5±3.4	12.8±3.2

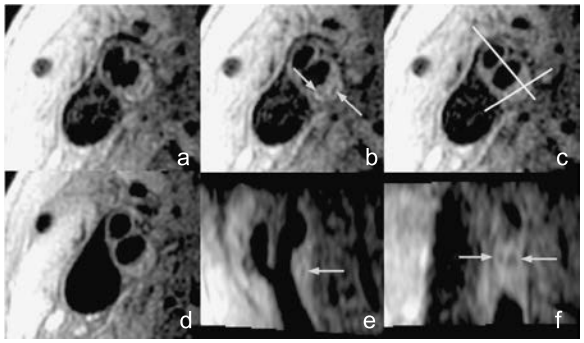

Figure 1. Black-blood images of a patient with atherosclerotic plaque in the right CA: a–c: Three contiguous slices from 3D data set; d: 2D image at the same location; e,f: oblique views reformatted from 3D data along planes shown on image (c). Arrows indicate calcifications. (*View this art in color at www.dekker.com.*)

plaques (Figure 1). More details of plaque structure were seen on 3D images due to reduced slice thickness (Figure 1). The 3D method showed strong dependence of blood suppression on the slab thickness (Figure 2). For thick slabs (>60 mm), severe flow artifacts were observed. These findings confirm the fact that an increased flow sensitivity of the 3D DIR-FSE technique is caused by incomplete outflow from the re-inverted volume. An optimal slab thickness for sufficient blood suppression and image SNR was found to be 16–24 mm.

Conclusions: A decrease of slice thickness results in marked improvement of the visualization of plaque structure on 3D images. The most advantageous application of the 3D method can be the precise morphometry of the vessel wall and plaque components in a selected artery segment.

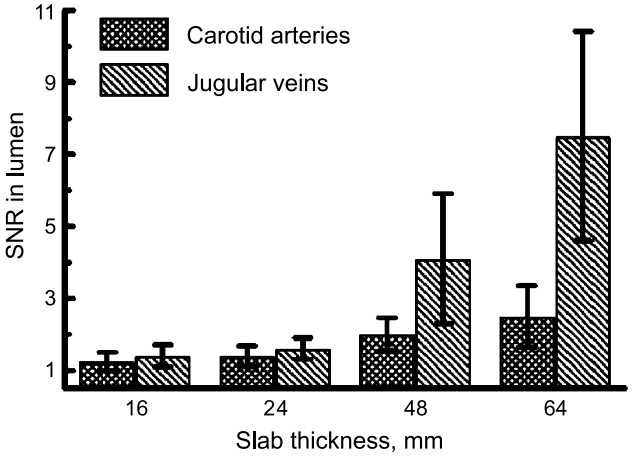

Figure 2. Comparison of flow suppression for 3D DIR-FSE scans with variable slab thickness.

Copyright © Marcel Dekker, Inc. All rights reserved.

Marcel Dekker, Inc.
270 Madison Avenue, New York, New York 10016

ORDER REPRINTS

REFERENCES

Crowe, L., et al. (2003). *JMRI* 17:572–580.
Fayad, Z. A., Fuster, V. (2000). *Ann. N.Y. Acad. Sci.* 902:173–186.
Luk-Pat, G. T., et al. (1999). *MRM* 42:762–771.
Stuber, M., et al. (2001). *MRM* 45:206–211.
Yuan, C., et al. (2001). *Radiology* 221:285–299.

205. Accurate Quantification of Mitral Valvular Flow in Healthy Subjects and in Patients with Regurgitation Using Three-Directional Velocity-Encoded MRI

Jos J. M. Westenberg, PhD,[1] Joost Doornbos, PhD,[1] Jeroen J. Bax, PhD,[2] Michel I. M. Versteegh, MD,[3] Mikhail G. Danilouchkine, PhD,[1] Gerda Labadie,[1] Rob J. van der Geest, MSc,[1] Hildo J. Lamb, PhD,[1] Eline F. Bruggemans, MD,[3] Albert de Roos, PhD, MD,[1] Robert A. E. Dion, PhD, MD,[3] Johan H. C. Reiber, PhD.[1]
[1]*Radiology, Leiden University Medical Center, Leiden, Netherlands,* [2]*Cardiology, Leiden University Medical Center, Leiden, Netherlands,* [3]*Cardio-Thoracic Surgery, Leiden University Medical Center, Leiden, Netherlands.*

Introduction: Echocardiography, the current tool for diagnosing mitral valve (MV) regurgitation, is not accurate when quantifying MV-flow. With MRI, flow quantification is possible, but the conventional sequence (1-directional (1-dir) velocity-encoded (VE) MRI) (Kayser et al., 1997) is not adapted to the motion of the MV during contraction, and therefore the flow is not acquired at the MV during the whole cardiac cycle. The S-Track method with a motion-adapted acquisition plane using prospective triggering (Kozerke et al., 1999) can not be used if flow quantification during the complete cardiac cycle is desired.

Purpose: In this study, a new method for quantifying MV-flow is presented, using 3-dir VE MRI. The flow going through the MV will be measured for the complete cardiac cycle.

Methods: MRI was performed on a 1.5 T scanner (ACS-NT15 Gyroscan with the Powertrack 6000 gradient system; Philips Medical Systems, Best, The Netherlands), using the body coil for transmission and a five element phased array cardiac-coil placed on the chest for signal reception. A radial stack of 6 MR acquisition planes is positioned on the left ventricle (Figure 1), with the radial axis parallel to the long-axis. For each plane, a 3-dir VE acquisition is performed with Venc=100 cm/s in all three directions. Slice thickness was 8 mm, Field-of-View= 370 mm (60% rectangular), scan matrix=128×102, with voxels of $2.89 \times 2.89 \times 8.0$ mm. The flip angle=10°, TR/TE=5.8/3.5 and NSA=2. Retrospective cardiac synchronization was used, 30 time phases were reconstructed for one cardiac cycle. Typical examination time was 9–12 minutes, depending on the heart rate.

Velocity vector fields are determined of the intraventricular blood flow for each of the 30 time phases during the cardiac cycle. The position of the MV-plane in this vector field is indicated manually. The MV-flow is determined from the velocity values perpendicular to this MV-plane.

Volume flows determined with 3-dir VE MRI and 1-dir VE MRI are compared with the flow through the

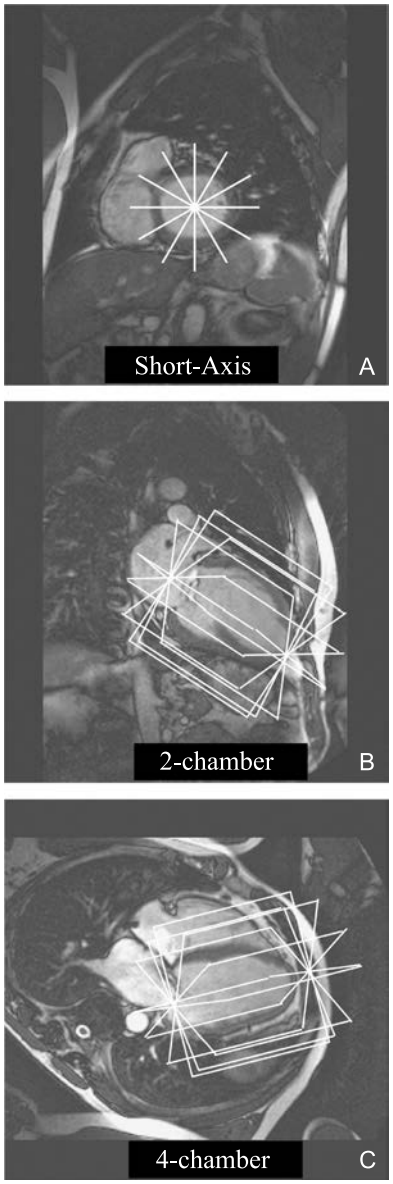

Figure 1.

Copyright © Marcel Dekker, Inc. All rights reserved.

ORDER REPRINTS

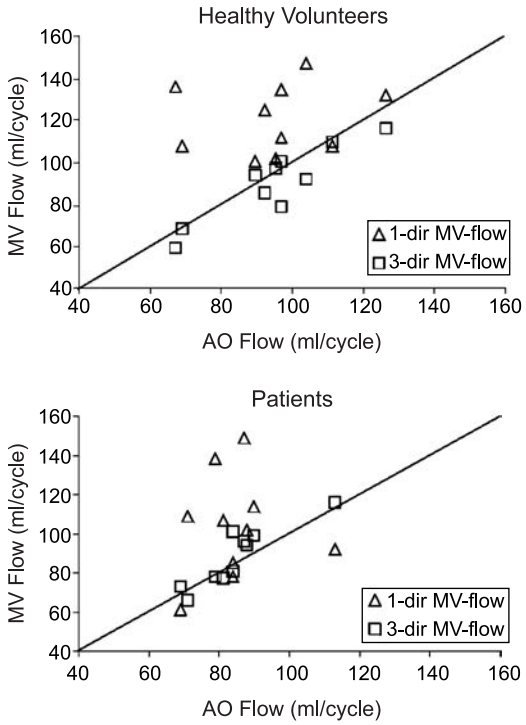

Figure 2.

ascending aorta (AO). Ten healthy volunteers without regurgitation and ten patients suffering MV-regurgitation are included. Reproducibility and accuracy are examined by studying inter- and intra-observer variations.

Results: 1-dir VE MRI shows a mean overestimation ($p<0.01$) of 25 ml/cycle, compared to the AO-flow. Correlation is very poor ($r_P=0.15$, $p=0.68$). 3-dir VE MRI shows no over/underestimation and there is good correlation ($r_P=0.91$, $p<0.01$ for the volunteers, $r_P=0.90$, $p<0.01$ the patients) (Figure 2). Intra- and inter-observer variations are small (0.9 ml/cycle and 1.3 ml/cycle) and not statistically significant. The regurgitation flow fractions were found to be in a range of 3%–30% for these patients.

Conclusions: With 3-dir VE MRI, MV-flow quantification is accurate and reproducible. This is a valuable tool for diagnosing patients undergoing MV valvuloplasty or replacement.

REFERENCES

Kayser, H. W.M., et al. (1997). MR velocity mapping of tricuspid flow: correction for through-plane motion. *J. Magn. Reson. Imaging* 7:669–673.

Kozerke, S., et al. (1999). Heart motion adapted cine phase-contrast flow measurements through the aortic valve. *Magn. Reson. Med.* 42:970–978.

206. Practical Guidelines on High-Resolution Black-Blood MRI of Carotid Atherosclerotic Plaque Using 3T Magnetic Field

Vasily L. Yarnykh, PhD,[1] Cecil E. Hayes, PhD,[1] Ann Shimakawa,[2] Masahiro Terashima, MD, PhD,[3] Patricia K. Nguyen, MD,[3] Jean H. Brittain, PhD,[2] Michael V. McConnell, MD,[3] Chun Yuan, PhD.[1] [1]*Radiology, University of Washington, Seattle, WA, USA,* [2]*GE Medical Systems, Menlo Park, CA, USA,* [3]*School of Medicine, Stanford University, Stanford, CA, USA.*

Introduction: Since introduction of 3T scanners into clinical practice, advantages of high-field MRI have been extensively explored in many radiological applications. In the imaging of carotid atherosclerotic plaque, no systematic studies were conducted in order to evaluate benefits and limitations of 3T and suggest optimal protocols.

Purpose: To optimize a protocol for black-blood carotid MRI at 3T and compare the performance of carotid imaging on 1.5T and 3T scanners.

Methods: Experiments were conducted on 1.5 and 3T scanners (GE Medical Systems) using four-element phased-array coils with the identical geometry. The multicontrast protocol included T_1-, T_2- and proton density (PD)-weighted 2D black-blood fast spin-echo sequences with following parameters TR(ms)/TE(ms)/echo train: 800/10/10 for T_1-, 2500/50/12 for T_2-, and 2500/9/12 for PD-weighted scans. For black-blood imaging with long TR (PD- and T_2-weighted), a multislice double inversion-recovery (DIR) method (Yarnykh and Yuan, 2003) was used with 4 slices per TR. Inversion times (TI) were 272 ms for 1.5T and 281 ms for 3T, which correspond to blood $T_1=1200$ ms at 1.5 and 1550 ms at 3T (Noeske et al., 2000). T_1-weighted images were obtained using single-slice DIR with TI=335 and 349 ms for 1.5T and 3T respectively. For each contrast weighting, different combinations of the matrix size (MTX=256,384,512) and the number of excitations (NEX=1,2) were tested. All images were obtained with FOV=14–16 cm and slice thickness of 2 mm. Comparison of 1.5T and 3T performance was outlined from the identical examinations of six healthy volunteers. Optimized clinical 3T protocol (see below) was tested in four patients with advanced carotid atherosclerosis.

Results: The multislice DIR method provided time-efficient black-blood imaging without exceeding SAR limits at 3T. Flow suppression was identical at 1.5

Copyright © Marcel Dekker, Inc. All rights reserved.

ORDER REPRINTS

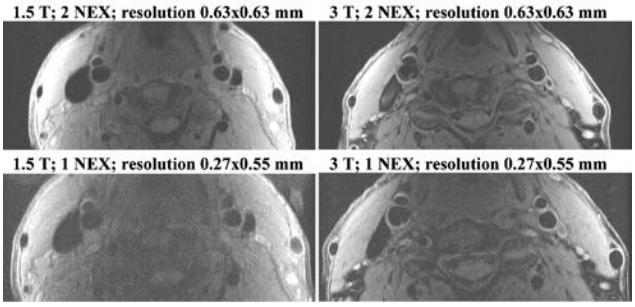

Figure 1. Comparison of high-resolution T_1-weighted black-blood images of carotid arteries obtained from a healthy volunteer at 1.5 and 3T with different in-plane resolution and NEX. Top row: FOV/MTX = 16 cm/256; bottom row: FOV/MTX = 14 cm/512.

and 3T for both single- and multislice DIR. An average factor for SNR increase at 3T vs. 1.5T was about 1.6±0.3. Detailed SNR compatisons are presented in another submission from our group (Terashima, et al.). Observed SNR gain at 3T was less than the theoretically expected value (2.2 times) based on field increase and impedance of our coils. We address this issue to increased tissue saturation at 3T due to longer T_1's. SNR improvement at 3T was sufficient to use NEX = 1 and the same or higher resolution. Figure 1 illustrates the fact that SNR at 3T obtained with twice-increased resolution and NEX = 1 is comparable to a standard 1.5T protocol (MTX = 256, NEX = 2). SNR limitations at 3T were more restrictive for T_2-weighted imaging, where an acceptable image quality could not be achieved with MTX = 512 and NEX = 1. Taking into account the need of identical resolution for all contrast weightings, we recommend a fast 3T protocol for routine applications with NEX = 1 and in-plane resolution ~0.4 mm, i.e. MTX = 384 and FOV = 16 cm (Figure 2).

Conclusions: Black-blood imaging of carotid arteries at 3T benefits from considerable increase of SNR. We developed a state-of-the-art protocol based on 3T advantages in combination with the time-efficient multislice DIR technique. Optimal use of a 3T scanner for carotid MRI provides either a 50%-reduction of scan time or simultaneous increase of resolution and reduction of scan time with a factor of 1.5, as compared to 1.5T imaging.

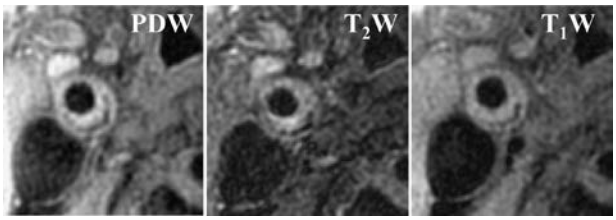

Figure 2. Multicontrast images of atherosclerotic plaque obtained at 3T with NEX = 1 and in-plane resolution of 0.42 mm. Scan time was 1 min per four slices for T_2-weighted and PD-weighted scans, and 25 s per slice for a T_1-weighted scan. Images show semicircular area of calcification (dark) and variable signal intensity within the plaque.

REFERENCES

Noeske, R., et al. (2000). *MRM* 44:978–982.
Yarnykh, V. L., Yuan, C. (2003). *JMRI* 17:478–483.

207. In-Vivo Molecular MR Imaging of Acute Coronary Thrombosis Using a Fibrin-Targeted Contrast Agent

René M. Botnar,[1] Arno Buecker,[2] Andrea J. Wiethoff,[3] Edward C. Parsons, Jr,[3] Marcus Katoh,[2] Randall B. Lauffer,[3] Robert M. Weisskoff,[3] Rolf W. Gunther,[2] Warren J. Manning,[1] Elmar Spuentrup.[2] [1]*Cardiovascular Division, Beth Israel Deaconess Medical Center and Harvard Medical School, Boston, MA, USA,* [2]*Department of Radiology, RWTH-Aachen, Aachen, Germany,* [3]*EPIX Medical Inc, Cambridge, MA, USA.*

Introduction: The majority of acute coronary syndromes are believed to result from coronary plaque rupture with subsequent thrombosis. MR thrombus imaging has been demonstrated in large quasi static vessels with regard to presence, age and thrombus composition (red cells). However, early thrombus formation in acute coronary syndromes or during acute in-stent thrombosis predominantly results in platelet/fibrin rich white thrombi. Thus, early detection of white thrombus may be beneficial both for diagnosis and treatment of patients that present with signs of acute in-stent thrombosis or non ST-segment elevation acute coronary syndromes. With the advent of fibrin-binding molecular MR contrast agents and advances in MR coronary artery imaging technology, direct imaging of coronary thrombosis may now be possible.

Purpose: We sought to test the feasibility of direct imaging of acute coronary thrombus using a Gadolinium (Gd) labeled fibrin-binding peptide, EP-2104R (EPIX Medical Inc., Cambridge, MA) in an in-vivo swine model of coronary thrombosis.

Methods: Thrombi were engineered with human fibrinogen and blood. Three thrombi were delivered under x-ray guidance to the right coronary artery (RCA), left anterior descending (LAD), and left circumflex (LCX) of two swine (50 kg, F). Subsequently, non-contrast

Copyright © Marcel Dekker, Inc. All rights reserved.

ORDER REPRINTS

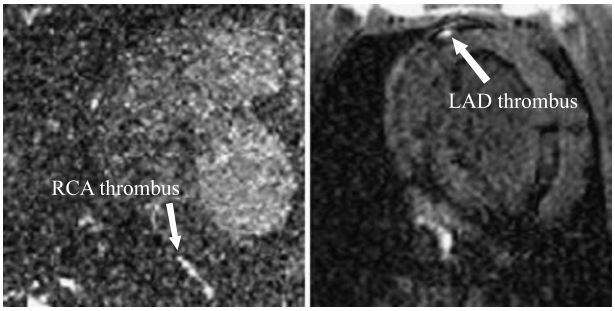

Figure 1.

enhanced MRI of the entire heart was performed using an ECG triggered and navigator gated inversion recovery (IR) 3D gradient echo (TFE) sequence. Imaging parameters of the T1 weighted black blood IR-TFE sequence included FOV=320 mm, matrix=256*256, in-plane resolution=1.25*1.25 mm, slice thickness=3 mm, acquisition window=50 ms, TR/TE=4.7 ms/1.4 ms, partial echo, flip angle=30°, inversion time=285 ms (@ 90 bpm), and number of slices=20–30. Imaging time was ~10–12 minutes. All data were acquired in late-diastole with the navigator placed on the dome of the right hemidiaphragm using a 5 mm gating window. Following non-contrast enhanced MRI, systemic injection of EP-2104R (7.5 ìmol/kg) was performed through the right ear vein and MRI was repeated until 2 hours post injection. After completion of MRI, both pigs were imaged using a contrast-enhanced 16-row multi detector (MD) CT. Following MDCT, autopsies were performed, and thrombi were excised for analysis.

Results: 90 minutes after contrast injection, all three thrombi (RCA, LAD, LCX) were visible on T1 weighted IR MR images (Figure 1). Presence and location of coronary thrombus was confirmed by MDCT, x-ray angiography and autopsy. Analysis of excised thrombi by mass spectrometry confirmed the expected Gd concentration.

Conclusion: We successfully demonstrate the feasibility of in-vivo molecular imaging of acute coronary thrombus using a fibrin-targeted contrast agent and systemic contrast injection. Potential applications include detection of acute coronary syndromes, atrial fibrillation, and suspected pulmonary embolism.

208. Three-Dimensional Displacement-Encoded Multi-Slice MRI of the Mouse Heart

Wesley D. Gilson, Zequan Yang, Brent A. French, Frederick H. Epstein. *Departments of Biomedical Engineering and Radiology, University of Virginia, Charlottesville, VA, USA.*

Introduction: Displacement-encoded imaging with stimulated echoes (DENSE) is a high resolution MRI technique for mapping intramyocardial function (Aletras et al., 1999). Short-axis DENSE has been used to measure 2D myocardial strain in normal and post-infarct mice (Gilson et al., 2002). However, since the heart contracts along its long axis as well as its short axis, a comprehensive measurement would encompass three dimensions.

Purpose: The purpose of this study was to develop a three-dimensional displacement-encoded multi-slice sequence and use it to measure the 3D mechanics at high spatial resolution in the mouse heart.

Methods: A multi-slice DENSE pulse sequence (Gilson et al., 2003) was developed on a 4.7 T scanner to study systolic function. The sequence was designed to apply the displacement-encoding gradient along the frequency-encoding direction for in-plane imaging and along the slice-select direction for through-plane imaging. For in-plane imaging, displacement encoding was performed in both orthogonal directions by swapping the direction of frequency encoding. Phase reference data with no displacement encoding was also acquired.

Three distinct echoes are present in a DENSE experiment: the desired displacement-encoded echo and two artifact-generating echoes (a complex conjugate echo and an echo due to T1-relaxation). We employed cosine and sine modulation to eliminate (CANSEL) (Epstein et al., 2002) these artifact-generating echoes independent of image resolution and displacement-encoding direction. The significance of this approach is that low displacement-encoding strengths can be used to avoid phase wrapping. Therefore, absolute rather than relative displacement can be measured. Also, through-plane displacement-encoding of short-axis images is feasible using this technique.

Three C57Bl/6 mice were imaged using multi-slice DENSE. During imaging, mice were anesthetized using 1% isoflurane in O_2, temperature was maintained at 37°C, and heart rate was monitored continuously. Imaging was performed using a quadrature RF coil and ECG gating. Three end-systolic short-axis images (basal, mid-ventricular, and apical) were acquired using multi-slice DENSE. Imaging parameters were FOV=30 mm, matrix=128×128, thickness=1 mm, flip angle=90°, TE=3.1 ms, TR=800 ms, and averages=2. The displacement-encoding strength was 0.64–0.85 cycles/mm for in-plane imaging and 0.5 cycles/mm for through-plane imaging.

Copyright © Marcel Dekker, Inc. All rights reserved.

ORDER REPRINTS

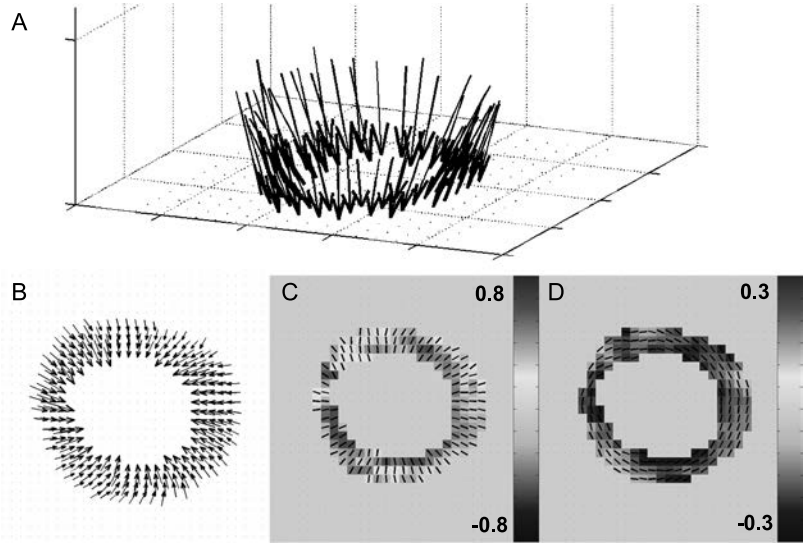

Figure 1. Displacement and strain maps for a basal short-axis slice taken from a three-dimensionally displacement-encoded multi-slice DENSE data set. (A) 3D vector displacement map with perspective favoring longitudinal motion. (B) 2D in-plane vector displacement map (with different scale than (A)). First (C) and second (D) in-plane principal strain maps. (*View this art in color at www.dekker.com.*)

DENSE raw data were combined as described in Epstein et al. (2003) to suppress the complex conjugate and T1-relaxation echoes. Magnitude- and phase-reconstructed images were created from the combined raw data. The phase-reconstructed images were background phase corrected, combined, and used to compute 3D displacement maps. For each slice, principal (E1 and E2), radial (Err), and circumferential (Ecc) strains were computed from 2D in-plane displacements using finite element methods. Also, net twist angle and torsion were computed.

Results: Example data from a short-axis basal slice are shown in Figure 1. A subsampled 3D displacement map is shown in (A), with a perspective favoring longitudinal displacement. The 2D in-plane displacements from the same short-axis slice are shown in (B) with a different scale than in (A). Corresponding in-plane principal strain maps (C and D) exhibit a gradient of strain from epicardium to endocardium. Mean displacements, twist angle, Err and Ecc are summarized in Table 1. The end-systolic torsion from linear regression ($R=0.9$) of net twist angles was $1.35\pm0.24°$/mm. Total scan time was approximately 50 minutes per mouse.

Conclusions: Three-dimensional displacement-encoded multi-slice MRI can provide a fairly comprehensive measurement of myocardial mechanics in mice at 4.7T in less than 1 hour. With the exception of manual segmentation, data analysis is automatic. Myocardial strains agree well with previously published values in mice (Epstein et al., 2002). Net twist and torsion values are similar to those previously reported (Kolandaivelu et al., 2001). Multi-slice DENSE should prove useful for studying murine models of heart disease.

Table 1. Mechanical measurements of systolic function in mouse hearts.

	Base	Mid-ventricle	Apex
Radial Displacement (mm)	0.31±0.03	0.39±0.04	0.37±0.09
Circumferential Displacement (mm)	0.07±0.02	0.13±0.05	0.23±0.06
Longitudinal Displacement (mm)	0.64±0.12	0.36±0.10	0.17±0.06
Net Twist Angle (°)	1.4±0.3	2.4±0.8	5.4±1.0
Radial Strain (Err)	0.266±0.03	0.38±0.04	0.23±0.05
Circumferential Strain (Ecc)	−0.131±0.011	−0.146±0.008	−0.154±0.035

Copyright © Marcel Dekker, Inc. All rights reserved.

ORDER REPRINTS

REFERENCES

Aletras, et al. (1999). *JMR* 137:247–252.
Epstein, et al. (2002). *MRM* 48 (2):399–403.
Epstein, et al. (2003). *ISMRM* 11:1645.
Gilson, et al. (2002). *ISMRM* 10:1685.
Gilson, et al. (2003). *ISMRM* 11:1635.
Kolandaivelu, et al. (2001). *ISMRM* 9:1866.

209. Diffusion Tensor MRI Delineates Specific Microscopic Structural Changes in Cardiomyopathic Syrian Hamsters

Junjie Chen,[1] Wei Liu,[1] Victor Song,[2] Stacy Allen,[3] Liz Lacy,[3] Samuel Wickline,[3] Xin Yu.[3] [1]*Department of Biomedical Engineering, Washington University, Saint Louis, MO, USA,*[2]*Department of Radiology, Washington University, Saint Louis, MO, USA,* [3]*Cardiovascular MR Laboratories, Washington University, Saint Louis, MO, USA.*

Introduction: The cardiomyopathic (CM) Syrian hamster is a well-characterized animal model of cardiomyopathy. The development of myocardial lesions in CM heart involves tissue fibrosis with collagen deposition and ultimately scar tissue calcification. Recent studies from our laboratory suggested that diffusion tensor MRI (DTMRI) may provide a rapid and nondestructive technique for characterizing microscopic changes in the remodeling myocardium after infarction (Chen et al., 2003). However, potential structural and functional differences between infarct scar tissue and cardiomyopathic scar tissue have not been elucidated.

Purpose: The utility of DTMRI for delineating microscopic cardiac lesions in CM Syrian hamster hearts was defined in this study.

Methods: Subjects—Myocardial structure of hearts from 6 CM hamsters (Bio T0-2 strain) and 6 normal hamsters (Bio F1-B strain) were characterized. After excision, hearts were retrogradely perfused with Krebs buffer and fixed with 10% formalin. On the day before imaging, hearts were rinsed and suspended in 1X PBS solution. Diffusion Tensor Imaging—DTMRI of fixed hearts was performed on a Varian 4.7T scanner. A multi-slice spin-echo sequence with diffusion sensitizing bipolar gradient was used. Imaging parameters were: TE, 45 msec; TR, 2.6 sec, b-value, 769 s/mm^2. Image resolution was 59 μm $\times$ 59 μm $\times$ 1 mm. Data Processing—Three eigenvalues of the diffusion tensor, the fractional anisotropy (FA) and the helix angle of the primary eigenvector were calculated to analyze diffusion magnitude, diffusion anisotropy and fiber orientation respectively. Myocardial fibrous scar tissue were defined as zones with signal intensity <1 SD below the mean intensity of the whole slice on T2-weighted image. Histology—Following the DTMRI study, hearts were sliced in 1 mm increments from base to apex along the LV long-axis to enable direct correlation of slice locations between MRI and histological analysis. Slices were stained with picrosirius red for collagen and Van Kossa for identification of myocardial calcification.

Results: Decreased water diffusivity and increased diffusion anisotropy were observed in fibrosis scar tissue of CM hearts (Figure 1a and 1b). The primary, secondary, and tertiary eigenvalues, normalized by the mean eigenvalue of the surrounding PBS solution, were 0.68 ± 0.03, 0.52 ± 0.06, and 0.43 ± 0.06 respectively in normal myocardium, 0.62 ± 0.05, 0.44 ± 0.04, and 0.33 ± 0.05 in scar tissue ($p<0.05$ compared to normal). FA was 0.24 ± 0.05 in normal myocardium, and 0.31 ± 0.06 in scar tissue.

The transmural variations of helix angle of both CM and normal hearts demonstated continuous transition from $+60^\circ$ at endocardium to -40° at epicardium. No significant difference of angular dispersion was observed between CM and normal myocardium.

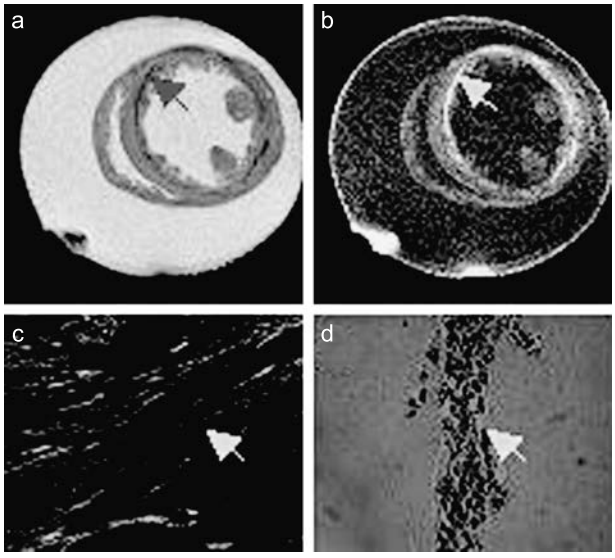

Figure 1. Scar tissue (arrows) in CM heart. (a) Decreased teritary eigenvalue of diffusion tensor (b) Increased FA (c) Deposited collagen fiber (orange and yellow) viewed under circularly polarized light at 200X (d) Calcium deposition delineated by Van Kossa staining. (*View this art in color at www.dekker.com.*)

Copyright © Marcel Dekker, Inc. All rights reserved.

ORDER REPRINTS

Picrosirius staining revealed that the mean orientation of collagen fibers in scar tissue aligned with that of adjacent myocytes (Figure 1c).

Conclusion: The transmural shift of fiber orientation was similar in normal and CM hearts, which accorded with previous findings in post-infarct rat hearts (Chen et al., 2003). However, contrary to *increased* water diffusivity and *decreased* diffusion anisotropy in scar tissue of post-infarct hearts, we observed *decreased* water diffusivity and *increased* diffusion anisotropy in lesions of CM hearts. The preserved fiber orientation reflects a well-organized structure of deposited collagen fiber in scar tissue. These densely deposited collagen fiber and excessive calcium deposition (Figure 1d) in scar tissue may have further restricted water diffusion, and therefore, lead to increased diffusion anisotropy. This study indicates that DTMRI is sensitive to different pathological processes of scar tissue formation in remodeling hearts as a consequence of cardiomyopathy or infarction.

REFERENCES

Chen, J., et al. (2003). *Am. J. Physiol.* 285:H946–H954.

210. Right Ventricular Pressure-Volume Loops and Pulmonary Pressure-Flow Relations in Patients with Pulmonary Hypertension: Assessment with an Interventional MRI Technique

Titus Kuehne,[1] Sevim Yilmaz,[1] Maarten Groenik,[2] Bernhard Schnackenburg,[3] Axel Bornstedt,[3] Eckart Fleck,[3] Eike Nagel,[3] Peter Ewert,[1] Ingram Schulze-Neick,[1] Peter E. Lange.[1] [1]*Congenital Heart Disease and Pediatric Cardiology, German Heart Institute, Berlin, Germany,* [2]*Cardiology, University Amsterdam, Amsterdam, Netherlands,* [3]*Cardiology, German Heart Institute, Berlin, Germany.*

Introduction: Pulmonary hypertension (PHT) is a common cause of morbidity and mortality in cardiology and a major factor complicating the management of children with congenital heart disease. Right ventricular function determines morbidity and mortality in these patients. Selective pulmonary vasodilation may be achieved using recently approved pulmonary vasodilators, thus reducing right ventricular afterload and improving transpulmonary blood flow. However, the precise effect of this treatment strategy on the components of right ventricular function and pulmonary vascular resistance have not been described in detail. Ventricular pressure-volume (PV) and pulmonary pressure-flow (PF) relations can give important insights into the inotropic state of the myocardium and vascular properties of the pulmonary bed. However, clinicians are confronted with the problem that current investigative approaches for measurement of cardiovascular physiology with conductance catheter, flow wires or thermodilution techniques are limited. Their use requires multiple catheter manipulation, are expensive (conductance catheter), are only representative for a small region of the pulmonary vasculature or are inaccurate.

Purpose: MRI is to date the gold standard to measure right ventricular volumes and quantitative pulmonary blood flow. In this study we used an interventional MRI technique to acquire simultaneously right ventricular volumes/pressures and pulmonary flow/pressures in patients with secondary pulmonary hypertension.

Methods: A total of 14 patients, age 41 ± 12, were studied. Eight patients with a hemodynamically not significant patent foramen ovale served as control. Six patients with either ventricular or atrial septal defect had secondary PHT. Patients were transferred after routine catheterisation into the MRI lab (Philips Intera CV, 1.5 Tesla). Vascular pressures were measured with a wedge catheter in the main pulmonary artery and in the right ventricle. The liquid filled catheter was connected to a Statham transducer. Analog signal was converted into digital signal with a pc-card and analyzed on a personal computer using a custom made software. The balloon catheter was temporary filled with carbon oxide for susceptibility based catheter visualization during balanced fast field echo (bFFE) MRI.

Simultaneously to the acquisition of pressure data, quantitative pulmonary blood flow and right ventricular volumes were measured using a velocity encoded cine (VEC) and bFFE technique. In order to minimize imaging time VEC MRI was acquired with SENSE. Used sequence parameters for VEC MRI were: TR = 14 msec, TE = 6 msec, VENC = 100–200, slice thickness = 8 mm, SENSE factor = 2, acquisition time 17–25 sec. Used sequence parameters for bFFE were: TR = 2.7 msec, TE = 2.6 msec, slice thickness 10 mm, SENSE factor = 2, NEX = 1.

After data acquisition, pressure and volume measurements were synchronized in time. Finally, data points were plotted in a xy-diagramm for construction of right ventricular pressure-volume and pulmonary pressure-flow relations.

Copyright © Marcel Dekker, Inc. All rights reserved.

ORDER REPRINTS

Results: All MRI measurements were completed in an average time of 32±10 minutes. Catheter manipulation within the MRI environment was unproblematic. There was good agreement between pressures acquired in the MRI environment and pressures measured in the catheter lab. Position monitoring of the catheter during MRI was achieved by slight susceptibility artifacts.

Normal pulmonary vascular resistance was measured in the controls (1.4±0.9 Wood Units*m2) but was significantly elevated in the PHT group (6.2±1.1 Wood Units*m2, p<.001). Slope and intercept of the PV-relation, a measure of incremental vascular resistance and effective outflow pressure, were significantly elevated in the PHT group when compared to control (p<0.001).

In patients with PHT there was a significant left and upward shift of the PV-curve in the PV-diagram indicative of an increased inotropic state of the myocardium due to chronic pressure overload.

Conclusions: MRI allows for minimal invasive acquisition of right ventricular pressure-volume loops and pulmonary pressure-flow relations. The results of this study imply that this technique has the potential to evaluate patients with pulmonary hypertension in a clinical setting.

211. Mapping Cardiac Contraction Timing in Man by High Temporal Resolution MRI Tagging: Early Onset and Late Peak of Shortening in the Lateral Wall

Jaco J. M. Zwanenburg,[1] J. T. Marcus,[1] Marco J. W. Götte,[2] Albert C. van Rossum.[2] [1]*Physics and Medical Technology, VU University Medical Center, Amsterdam, Netherlands,* [2]*Cardiology, VU University Medical Center, Amsterdam, Netherlands.*

Introduction: In cardiac resynchronization therapy (CRT) by biventricular pacing, prediction of (non-) responders is difficult but important since around 30% of the patients does not respond to the therapy. Mechanical synchronization is likely to be more important than electrical synchronization for effective CRT (Leclerq et al., 2002). Before patient data can be interpreted, the normal contraction timing should be assessed in healthy subjects.

Purpose: To map the cardiac contraction timing parameters in healthy human subjects by high temporal resolution myocardial tagging MRI. The onset time of circumferential shortening and the time to peak shortening were quantified.

Methods: Seventeen healthy subjects were studied (12 male, age 42±11 years). Myocardial tagging images with high temporal resolution (14 ms) were obtained using SSFP imaging (Zwanenburg et al., 2003) and a multiple breath-hold scheme. A stack of five short axis image planes was acquired. The time to mitral valve closure (T_{mvc}) and aortic valve closure (T_{avc}) relative to the ECG-R wave were obtained from a three-chamber cine with the same temporal resolution.

Circumferential strain (ε_c) was calculated using HARP (Osman and Prince, 1998) and averaged for 6 segments per slice: infero-septal (IS), antero-septal (AS), anterior (AN), antero-lateral (AL), postero-lateral (PL) and inferior (IN). The onset time of shortening (T_{os}) relative to the ECG-R wave was defined as the beginning of the down slope of the ε_c curve assessed by an automatic fitting algorithm. The time to peak shortening (T_{peakCS}) was expressed in % of systolic

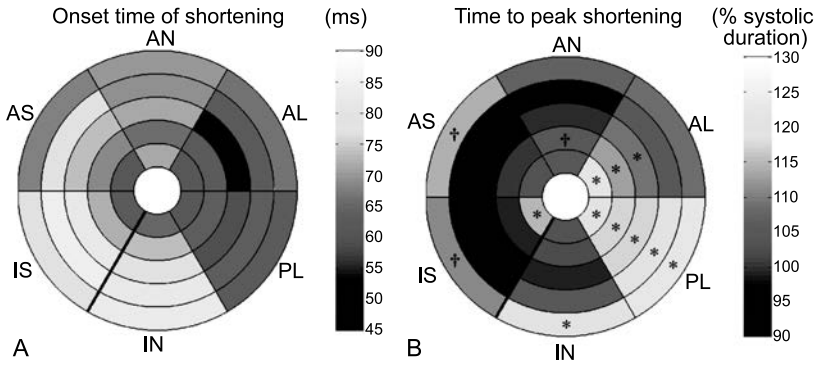

Figure 1. Data averaged per cardiac segment over all subjects. A: T_{os}. B: T_{peakCS}. Peak strain is reached significantly after aortic valve closure in the marked segments: *$p<0.01$, †$p<0.05$. (*View this art in color at www.dekker.com.*)

Copyright © Marcel Dekker, Inc. All rights reserved.

ORDER REPRINTS

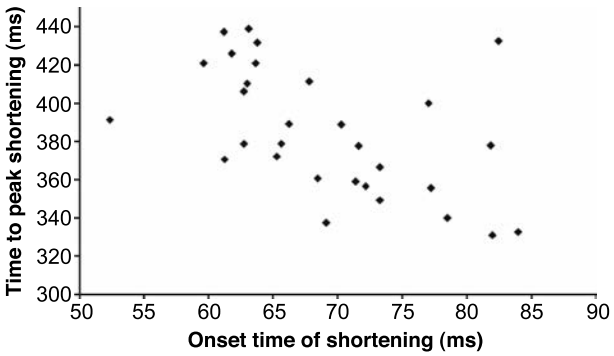

Figure 2. Scatterplot of time to peak shortening versus onset time of shortening for the 30 segments, averaged over all subjects. (*View this art in color at www.dekker.com.*)

duration in order to relate T_{peakCS} to the moment of aortic valve closure: $\%T_{peakCS} = (T_{peakCS} - T_{mvc})/(T_{avc} - T_{mvc}) \times 100\%$. A $\%T_{peakCS}$ larger than 100% indicated post-systolic shortening.

Results: The average onset time of shortening for each segment is shown in Figure 1a. Onset of shortening started 11±9 ms earlier in the lateral wall (AL+PL) compared to the septum (IS+AS) ($p<0.01$). The AN region was 7±14 ms earlier than the IN region ($p<0.05$). The apical slice was 7±12 ms earlier than the basal slice ($p<0.05$).

The regional time to peak shortening is presented in Figure 1b. Peak shortening was reached later in the lateral wall compared to the septum (115±4% vs. 102±4%, $p<0.01$). Segments with an earlier onset of shortening showed a longer shortening duration, yielding a negative correlation between T_{os} and T_{peakCS} ($r=-0.5$, $p<0.01$), see Figure 2.

Significant shortening after T_{avc} (defined as post-systolic shortening) was observed in 13 of the 30 segments (with average $\%T_{peakCS}=116\pm12\%$). In these segments shortening continued substantially from −17±4% at aortic valve closure to −20±4% at peak (the difference is 16±14% of the total shortening, $p<0.01$).

Conclusion: In the normal heart, onset of circumferential shortening starts in the anterior and lateral regions and propagates to the inferior and septal regions. Earlier onset of shortening is accompanied by longer duration of shortening. Significant post-systolic shortening occurs mainly in the lateral and basal segments. These data may contribute to the understanding of abnormal contraction timing patterns in candidates for cardiac resynchronization therapy.

Acknowledgment: Supported by the Netherlands Heart Foundation, grant 2000B220.

REFERENCES

Leclerq, C., Faris, O., et al. (2002). *Circulation* 106: 760.

Osman, N. F., Prince, J. L. (1998). Proc. SPIE Med Imag Conf., San Diego; 142.

Zwanenburg, J. J.M., Kuijer, J. P.A., et al. (2003). *Magn. Reson. Med.* 49:722.

212. Effects of Dobutamine Stress on Manganese-Enhanced MRI of Pig Myocardium

Rolf Eriksson, BSc, Lars Johansson, Tomas Bjerner, MD, PhD, Håkan Ahlström, MD, PhD. *Department of Radiology, Uppsala University, Uppsala, Sweden.*

Introduction: Manganese is a metallic element that forms ions with paramagnetic properties (Mn^{2+}). Mn^{2+}-ions have similarities to Ca^{2+}-ions and have a high affinity for cell-membrane calcium channels. Since Mn^{2+}-ions persist in myocardial tissue for a long time after injection there are indications that they could be used to detect transient myocardial ischemia by means of myocardial perfusion imaging combined with physiological or pharmacological stress. It has earlier been shown that manganese ions persist in tissue for more than an hour (Bremerich et al., 2000; Hu et al., 2001), that there is a difference between uptake in normal and infarcted myocardium (Bremerich et al., 2000) and that the uptake of Mn^{2+}-ions is increased in rat myocardium during dobutamine infusion after a $MnCl_2$ infusion over 30 minutes (Hu et al., 2001).

Purpose: The purpose of this study was to examine if the contrast effect of Mn2+-ions on pig myocardium was affected by dobutamine stress.

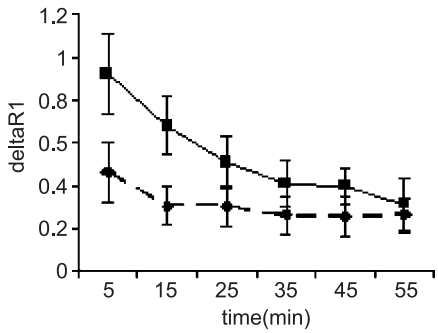

Figure 1.

Copyright © Marcel Dekker, Inc. All rights reserved.

ORDER REPRINTS

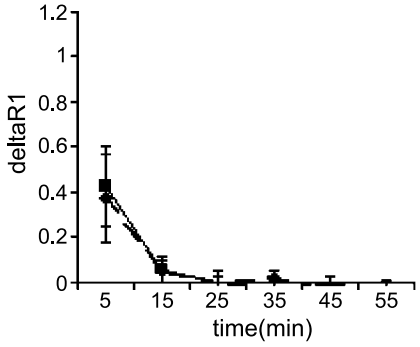

Figure 2.

Method: Twelve pigs were used for this study. The animals were divided into two groups (six in each group). In one group MnCl2 was injected at rest and in the other during dobutamine stress. 15 umol contrast agent/kg bodyweight was used (clinical dose is usually 5–10 umol/kg). The stress was induced by infusing 10 ug dobutamine/kg bodyweight/minute. Then the infusion rate was increased by 10 ug dobutamine/kg bodyweight/minute every two minutes until the product of heart rate and systolic blood pressure exceeded two times the rest value. A look-locker sequence with an initial 180° pulse followed by seventy 6° pulses (starting at 14 ms and every 42 ms thereafter) was used to create short-axis images of the heart at baseline (before contrast injection)) and 5, 15, 25, 35, 45 and 55 minutes post injection. For evaluation the data was fitted to a mono-exponential T1-function using DimWiew software (copyright Atle Björnerud, Oslo, Norway). R1 (1/T1) was calculated from the fit. R1 was measured in blood and two different parts of the myocardium. The arterial systolic blood pressure was monitored in each pig to examine the individual response to dobutamine. Statistical significance between groups was determined by independent samples T-tests.

Results: Figures 1 and 2 depict the change in R1 in myocardium and blood respectively using pre-contrast injection values as reference. The dotted line represents MnCl2 without dobutamine stress while the filled line represents MnCl2 with dobutamine stress. Error bars describe the standard deviation of each group. A difference in relaxation time between the groups was noted up to 45 minutes after injection in the myocardium. In blood, no relaxation time differences were detected between the groups.

Discussion/Conclusion: These results indicate that the effect of manganese ions on relaxation time is enhanced by dobutamine stress. The reason for this enhancement is probably twofold as dobutamine affects both the myocardial perfusion and the activity of the myocyte calcium channels. The maintained R1 difference between rest and stress indicate that Mn^{2+}-ions may be used as a marker of transient ischemia.

REFERENCES

Bremerich, J., et al. (2000). Normal and infarcted myocardium: differentiation with cellular uptake of manganese at MR imaging in a rat model. *Radiology* 216:524–530.

Hu, T. C., et al. (2001). Manganese-enhanced MRI of mouse heart during changes in inotropy. *Magn. Reson. Med.* 46:884–890.

213. In Vivo Heating of Pacemaker Leads During MRI

Roger Luechinger,[1] Volkert A. Zeijlemaker,[2] Erik M. Pedersen,[3] Peter Mortensen,[3] Erling Falk,[3] Reto Candinas,[4] Firat Duru,[4] Peter Boesiger.[1] [1]*Biophysics, Institute for Biomedical Engineering, Zuerich, Switzerland,* [2]*Medtronic Bakken Research Center, Maastricht, Netherlands,* [3]*Skejby Sygehus, Aarhus, Denmark,* [4]*Cardiology, University Hospital, Zuerich, Switzerland.*

Introduction: The presence of a cardiac pacemaker is usually regarded as a contraindication for MRI due to safety reasons. Heating effects at the lead tip is one of the potential risks, so far only in-vitro data on heating effects are available.

Purpose: To study heating effects in a chronical pig model using standard length screw-in pacemaker leads at 1.5T.

Methods: Pacemaker systems with three active fixation leads were implanted in six 70 kg pigs. All leads were equipped with a T-type thermocouple as temperature sensor. The accuracy of the thermocouple and its influence on the heating was investigated in-vitro

Table 1. Total scantime and temperature increase.

Animal	Total scan time [min]	Atrium ΔT_{avg} [°C]	Ventricle ΔT_{avg} [°C]	Ventricle (outflow track) ΔT_{avg} [°C]
1	30	–	–	–
2	41	–	5.7*	5.4*
3	41	15.7	11.1	12.2
4	37	5.7	9.3	9.7
5	40	9.1	7.5	9.0
6	42	3.7	3.9	11.4

Copyright © Marcel Dekker, Inc. All rights reserved.

ORDER REPRINTS

Table 2. Impedance changes.

	Pre MRI	Post MRI	2 Weeks after MRI
Right atrial lead	492±57 Ω	516±29 Ω (+5.5%±6.2%)	575±86 Ω (+16.8%±9%)
Right ventricular lead	567±93 Ω	629±86 Ω (+11.5%±6.8%)	601±58 Ω (+7.5%±14.5%)
Right ventricular lead (Outflow track)	525±27 Ω	560±23 Ω (+6.9%±5.9%)	595±43 Ω (+13.6%±9.4%)

with a fiberoptic sensor. Four weeks after implantation of the leads MRI was performed. The pigs were placed in supine position with the heart at the isocenter of the scanner. TSE scans with a SAR-value of 3.8 W/kg were performed. The influence of position on heating was evaluated by moving one pig stepwise 40 cm out of the scanner. Pacing parameters like capture threshold and pacing impedance were measured after implantation, pre, during, and after MRI and two weeks after MRI. Troponin-levels were measured from blood samples taken before and 8 h after MRI. The animals were sacrificed two weeks after MRI and gross morphological and pathological examinations and histology of the regions around the lead tips were performed.

Results: The in-vitro validation of the thermocouple showed a good agreement with the fiberoptic sensor. The thermocouple leads showed no additional heating, compared with an identical lead with removed thermocouple. Significant heating effects could be seen in all animals and at all pacing positions. The temperature increased fast and reached a stable value in less than 15 sec. The overall scan times and temperature changes at the lead tip are shown in Table 1. Only part of the temperature measurements are available the first two animals due to broken thermocouples.

The changes of the pacing impedance are shown in Table 2.

Minor increases in stimulation thresholds were seen. However, they did not prevent further pacing of the heart. All Troponin tests were negative, indicating that no major heart tissue damage occurred. Pathology showed no clear evidence of heat-induced damage. Cell damage induced by the implantation could not be distinguished from potential cell damage induced by heating 2 weeks after MRI. No strong relation between measured temperatures and heat-induced inflammation could be found (Figure 1).

Discussion: MRI at 1.5T produces a temperature increase of more than 15°C at lead tips. It is known from simulation, that the heating drops fast with increasing distance from the lead tip. The temperature increase in the tissue circumventing the 2–3 mm thick scar tissue at the tip may therefore be reduced by more than a factor of two. Changes in the essential pacing parameters like capture threshold due to MRI were demonstrated. The location of implanted pacing leads and the position of the animal within the MRI-scanner may result in marked differences in heating. Despite the aim of introducing maximum heating effects, no specific heating related pathological changes were seen. Changes in the position of the pacemaker lead

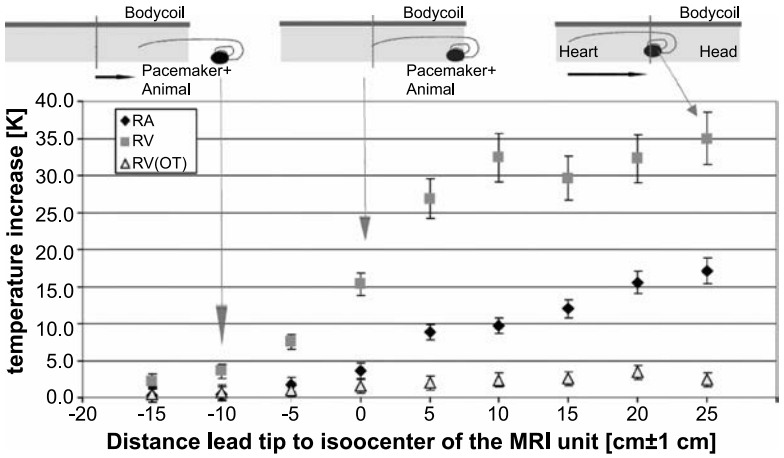

Figure 1. By moving the animal out of the scanner, it could be seen that as soon as part of the pacemaker lead was outside the body coil of the scanner, the temperature increase was reduced. (*View this art in color at www.dekker.com.*)

Copyright © Marcel Dekker, Inc. All rights reserved.

ORDER REPRINTS

tips in the direction orthogonal to the main magnetic field are, however, known to increase heating effects. Potential risk of tissue damage cannot be totally excluded. Reduction of the SAR-value by changing the MRI sequence and measuring e.g. lower extremities or head are likely to reduce the risk of heat-induced tissue damage.

214. Non-Invasive Non-contrast Cine Angiography Using Selective Excitation and Global Coherent Free Precession (GCFP)

Wolfgang G. Rehwald, PhD,[1] Enn-Ling Chen, PhD,[2] Raymond J. Kim, MD,[2] Robert M. Judd, PhD.[2] [1]*Duke Cardiovascular MR Center, Duke University and Siemens Medical Solutions, Durham, NC, USA,* [2]*Duke Cardiovascular MR Center, Duke University, Durham, NC, USA.*

Introduction: Conventional X-ray angiography allows visualization of both vessel morphology and blood flow. MR angiography (MRA) does not provide temporal information. We developed a new MR method based on a fundamentally new physical principle that produces dynamic images directly analogous to those of x-ray angiography.

Purpose: To describe a new physical principle which allows MRI to produce cine projection angiograms non-invasively, without a contrast agent, and without ionizing radiation.

Methods: The underlying concept of the new technique is that a condition of ''global coherent free precession'' (GCFP) can be created and maintained. In the GCFP state, excited protons continue to yield signal regardless of where they travel, even in the absence of additional radiofrequency (RF) excitation. The GCFP state requires that three fundamental conditions be met:

1) proton excitation must maintain a coherent phase (e.g. transmit exactly on resonance and set the phase increment of the transmitter to zero).
2) free precession must be maintained throughout 3D space (e.g. set the zeroth moment of all gradient waveforms to zero across TR).
3) phase accumulation due to motion must be avoided (e.g. set the first moment of all gradient waveforms to zero across TR).

Importantly, these GCFP conditions can be met while simultaneously achieving two additional goals. First, RF excitation pulses can be played every few milliseconds while the GCFP gradients play, effectively creating a continuous outward flow of excited protons. Second, projection images can be acquired using the same gradient waveforms used for RF excitation and GCFP. Thus the image data can be collected at the same time a new spin state is created within the human body: spatially-selective RF pulses produce a continuous stream of coherently excited blood which freely precesses as it flows through regions of space unaffected by the ongoing excitation. A pulse sequence satisfying these conditions was implemented on a 1.5T clinical MRI scanner (Siemens Sonata) and tested in 15 dogs and 3 volunteers. All images employed ECG gating, segmented k-space, and breath holding.

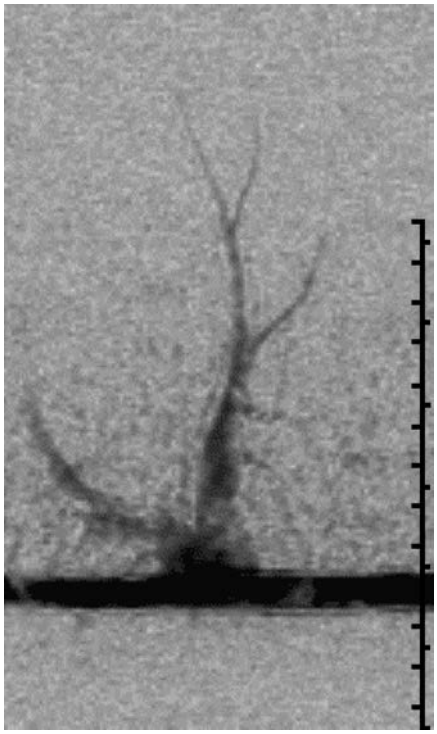

Figure 1.

Results: Figure 1 shows a representative movie of one cardiac cycle depicting blood flow into the pulmonary artery. Excited blood was seen to fill the pulmonary tree for a distance of approximately 11 cm (left-hand tick marks are 1 cm), and branch vessels as small as 1.5 mm in diameter were clearly visualized. Signal-to-noise ratios in major arteries was typically 80–100. Figure 2 summarizes in vivo filling distances as seen in a single cardiac cycle in selected arteries.

Conclusions: Selective RF excitation combined with global coherent free precession results in a unique

Copyright © Marcel Dekker, Inc. All rights reserved.

ORDER REPRINTS

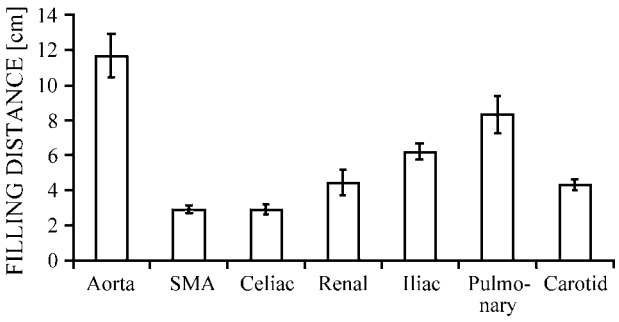

Figure 2.

spin state within the human body that has not been previously described. By continuously maintaining this spin state magnetic resonance images directly analogous to those of invasive catheterization can be acquired non-invasively and without a contrast agent.

215. Myocardial Perfusion Measurements by Spin-Labeling Under Different Vasodynamic States

Christian M. Wacker, Florian Fidler, Christian Dueren, Peter M. Jakob, Axel Haase, Wolfgang R. Bauer. *Medical Clinics, Cardiology and Biophysics, University, Wuerzburg, Germany.*

Introduction: In recent years, most MRI approaches for perfusion assessment were based on first-pass techniques, which evaluate signal dynamics after application of contrast agent (CA). Perfusion then is obtained either qualitatively by empiric parameters or quantitatively by deconvolution of the concentration time curve. However, despite of its widespread use in myocardial perfusion imaging, the disadvantages of first pass techniques are well known, e.g. measurements are not easily repeatable and data have to be unfolded with an arterial input function.

Spin-labeling techniques exploit the labeling of the nuclear magnetization of water protons either by direct preparation of inflowing spins or by specific preparation of the imaging slice and leaving the inflowing spins in thermo-magnetic equilibrium. In both cases water is used as a free diffusible CA.

Purpose: The objective of this study was a quantitative analysis of myocardial perfusion assessed by spin-labeling at rest and after vasodilation and demonstration of the coronary autoregulation in the human heart at 2 Tesla.

Methods: Pulse sequences were implemented on a 2 Tesla whole body scanner (Bruker, Ettlingen, Germany) with a maximal gradient strength of 31 mT/m and a rise time of 600 ìsec. For determination of T_1 we implemented a fast ECG-gated saturation recovery FLASH sequence. Between a 40 ms spin preparation consisting of five 90° pulses followed by spoiler gradients and a FLASH readout a progressing recovery delay T_S leads to set of images, which allows quantification of appropriate T_1. One image for equilibrium magnetization and nine images with progressing recovery delays T_S (100, 200, 300, 400, 600, 800, 1000, 1200 and 1400 ms) were obtained. For each T_S an initial ECG-trigger delay was adjusted automatically by heart rate to acquire end-diastolic images. The readout module was a centric reordered FLASH image with phase rewinder ($T_R/T_E/\alpha$/FOV/SL/Matrix/SW = 2.9 ms/1.4 ms/5°/300 mm/12 mm/128×80/780 Hz per pixel). Acquisition time per image was 230 ms. Spin preparation was done globally and slice-selective. The global preparation saturated the whole probe, while slice selective preparation labeled the readout slice down to the apex of the heart with a 60 mm saturation slab.

16 healthy volunteers (13 male/3 female, aged 27 ± 9 years) were examined after being informed about the protocol and possible side effects of adenosine. In 10 volunteers measurements were performed at rest and while applying adenosine with a dose of 0.14 mg/kg/min via an antecubital vein. In 7 volunteers exams were done under oxygen breathing within 15 to 20 minutes and while the subject inhaled room air. One volunteer underwent both adenosine and oxygen protocol within one exam. Total examination time for each volunteer was about 45 min in a preselected single slice.

Results: Quantitative perfusion P was calculated as 2.3 ± 0.8 ml/g/min (rest), 4.2 ± 1.0 ml/g/min (adenosine)

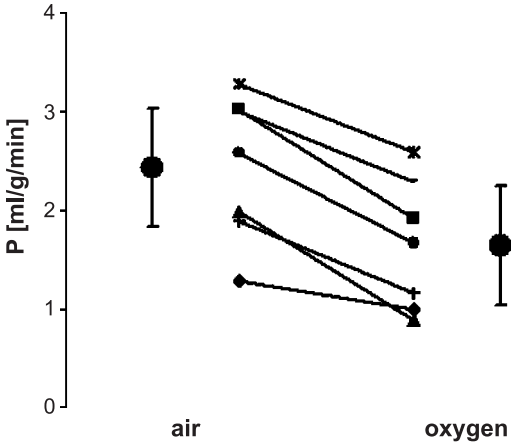

Figure 1.

Copyright © Marcel Dekker, Inc. All rights reserved.

ORDER REPRINTS

and 1.6±0.6 ml/g/min (oxygen, Figure 1), respectively. T_1 of skeletal muscle and fat did not change significantly. Myocardial T_1 remains almost constant under extended oxygen consumption in the limits of 1389±60 ms (rest) and 1351±65 ms (oxygen).

T_1 of left ventricular blood pool decreased from 1709±101 ms (rest) to 1423±61 ms (oxygen) ($p<0.0005$) whereas T_1 of right ventricular blood did not change significantly (1586±126 ms and 1558±150 ms, $p=0.7$).

Conclusions: The presented technique for quantification of myocardial perfusion is an alternative to contrast agent-based methods. The spin labeling method is noninvasive and easily repeatable and it could therefore become an important tool to study changes in myocardial perfusion under different vasodynamic states.

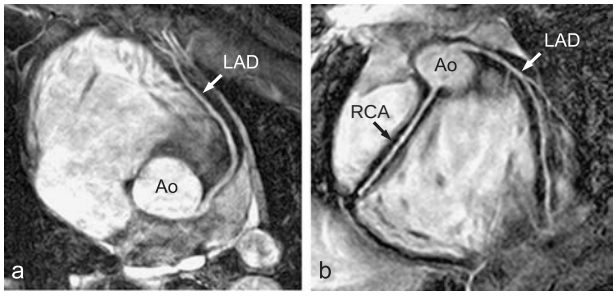

Figure 1. 3D coronary angiograms obtained with a real-time adaptive trigger delay for data acquisition during cardiac rest of mid-diastole. a) Left anterior descending artery (LAD). b) Example of a right coronary artery (RCA) and LAD with several smaller branches. Ao: aorta.

216. Real-Time Trigger Delay Adaptation in Coronary MRA

Michael E. Huber, Martin Buehrer, Sebastian Kozerke, Peter Boesiger. *Institute for Biomedical Engineering, University and ETH Zurich, Zurich, Switzerland.*

Introduction: Data acquisition in coronary MRA is commonly limited to the intrinsic cardiac rest period during mid-diastole (Kim et al., 2001; Wang et al., 1999). Therefore, after R-wave detection by a vector-ECG, the data sampling is delayed by a predefined, heart-rate dependent trigger delay. However, during the several minutes of scan time, the heart rate of the subject can vary considerably, which directly influences the position of the rest period within the cardiac cycle. This temporal shift of the rest period towards systole or late diastole is not considered in conventional protocols, since for each patient the expected heart rate and the corresponding trigger delay have to be set before the scan is started.

Purpose: To investigate the heart rate variability of ECG-triggered scans in volunteers and develop a real-time algorithm, which allows prospective adaptation of the trigger delay in coronary MRA based on the actual heart rate.

Methods: The actual heart rates during an ECG-triggered scan of 5 minutes were measured in eight healthy adult volunteers. The variability of the heart rate and its effect on the trigger delay adjustment for data acquisition during mid-diastole were evaluated.

Subsequently a real-time algorithm was implemented on a Philips Intera 1.5T system, which adapts the trigger delay for coronary MRA based on a heart-rate dependent formula (Stuber et al., 1999). The implementation was tested on three healthy volunteers, in combination with a 3D free-breathing navigator-gated steady-state free precession technique. Additional scan parameters were: 270 mm^2 field of view, 272×272 matrix, T2-prepared, fat-suppressed, TR=5.2 ms, TE=2.6 ms, flip angle=65°, 17 excitations per cardiac cycle. The duration of each single cardiac cycle and the adaptively applied trigger delay were stored for all measurements.

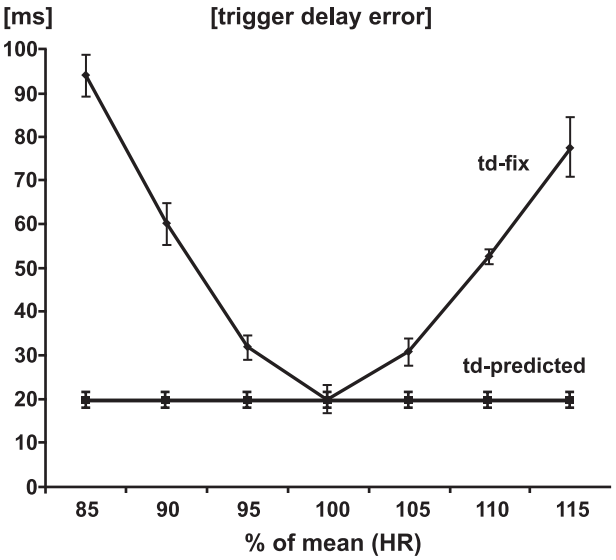

Figure 2. Conventionally, the trigger delay has to be set prior to the scan (td-fix), according to the expected average heart rate. This may lead to large trigger delay errors, if the heart rate is under- or overestimated (100%=average heart rate). Using the real-time trigger delay adaptation, the mean absolute trigger delay error (td-predicted) becomes independent of any estimation about the expected average heart rate.

Copyright © Marcel Dekker, Inc. All rights reserved.

ORDER REPRINTS

Results: The evaluation of the heart rate from the eight volunteers showed strong variations during the 5 minutes of scan time. On average, the difference of the maximal and the minimal heart rate was 25 bpm (stdev=9 bpm). As a consequence the corresponding heart-rate dependent trigger delay varied by 231 ms on average (stdev=108 ms).

The adaptive trigger delay algorithm was successfully applied in first in-vivo measurements. Example angiograms from two different subjects are given in Figure 1.

The evaluation of the average absolute error between the applied trigger delay and the theoretical (=based on the actual heart rate) trigger delay, obtained from the three measurements with the new adaptive algorithm is given in Figure 2.

Conclusions: An adaptive algorithm for coronary MRA was implemented and successfully tested in first in-vivo measurements. It enables the adaptation of the trigger delay during the scan, based on changes of the actual heart rate. Hence, pre-estimations of the expected average heart rate and its related optimal trigger delay are no longer required. Future work will focus on the improved accuracy of the current prediction algorithm.

REFERENCES

Kim, Y., et al. (2001). *JMRI* 14:383–390.
Stuber, M., et al. (1999). *Radiology* 212:579–587.
Wang, Y., et al. (1999). *Radiology* 213:751–758.

217. High Resolution Spiral MRCA with Real-Time Localization at 3T

Juan Santos,[1] Phillip Yang,[1] Charles Cunningham,[1] Krishna Nayak,[2] Bob Hu,[3] Michael McConnell,[1] Jean Brittain,[4] John Pauly.[1] [1]*Electrical Engineering, Stanford University, Stanford, CA, USA,* [2]*Electrical Engineering, University of Southern California, Los Angeles, CA, USA,* [3]*Cardiology, Palo Alto Medical Foundation, Palo Alto, CA, USA,* [4]*ASL West, GE Medical Systems, Menlo Park, CA, USA.*

Introduction: Previously we presented a system for MR coronary angiography (MRCA) that seamlessly integrates real-time localization with high-resolution multi-slice spiral imaging (Santos et al., 2002). This system allows switching between the different acquisition modes within a TR, increasing image localization precision and reducing total study times. While spiral MRCA can potentially benefit from higher SNR at higher magnetic fields, increased susceptibility-induced off-resonance and RF inhomogeneity must be managed effectively. In this abstract we describe the design and optimization of a new RF excitation and spiral gradient echo pulse sequence for coronary imaging at 3T.

Purpose: Develop and test optimized high resolution spiral MRCA with real-time localization at 3T.

Methods: One of the major difficulties of multi-slice MRCA is the localization of the coronary vessels. The image plane must contain the objects of interest at a particular phase of the cardiac and respiratory cycles. We used the ''virtual scanner'' real-time system architecture (Santos et al., 2002) to integrate a low resolution, high frame rate real-time localizer with a spiral based high resolution MRCA sequence. Once the plane of interest has been localized, the user can immediately switch to a high resolution acquisition. This provides excellent registration between the prescribed and the acquired image planes.

We have previously optimized our real-time sequence for 3T (Nayak et al., 2003) by using eight 8 ms spiral interleaves, dynamic linear shim and center frequency correction, and a short spectral-spatial RF pulse. Here we apply similar ideas to the design of the high-resolution spiral acquisition. RF Design—A spectral-spatial RF pulse that excites thin 3 mm slices with sharp slice profile was designed for the MRCA application. Thin slices were achieved using a 1-3-3-1 1.2 ms sublobe envelope with 4 G/cm amplitude and 4.8 ms total duration.

By using the method introduced by Zur (2000), where the RF sublobes oscillate in polarity, the unwanted bipolar excitation at 440 Hz was suppressed, and good fat suppression was achieved.

Spectral-spatial slice profile

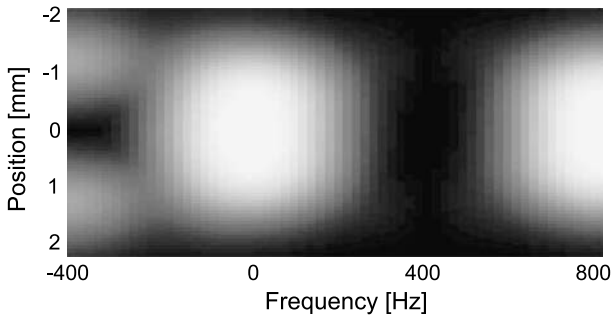

Readout—Breath hold duration and readout time are significant factors affecting acheivable image resolution. At 3T, susceptibility off-resonance effects limit readout time. We have designed a 24 interleave, 8 ms spiral readout to obtain 0.8 mm in plane resolution.

Copyright © Marcel Dekker, Inc. All rights reserved.

ORDER REPRINTS

This maintains comparable off-resonance sensitivity to the 16 ms readouts we typically use at 1.5T. The shorter readouts do increase the breath-hold duration for a particular resolution, but also allow the acquisition of more slices in a single breath-hold. Seven slices were acquired per breath-hold.

Control, reconstruction and display of the real-time and high resolution images was done with a 2.4 GHz Athlon workstation connected via ethernet to the scanner.

The system was implemented on a GE Signa 3.0T-VH/i system, with 40 mT/m maximum gradient amplitude and 150 T/m/s slew rate. A body coil was used for transmission and a 5-inch surface coil was used for reception.

Results: Six healthy volunteers were studied. Breath-hold duration of 22 seconds (20–24), total number of breath-holds of 5 (4–6), and mean scan time of 15 minutes (10–23) were required to visualize the coronary anatomy. Figure 1a-c represent different slices obtained from a single acquisition where (a) left circumflex, (b) left anterior descending with diagonal branch, and (c) left main arteries can be visualized. Figure 1d demonstrates the right coronary artery. Sharp and contiguous vessel border with wide anatomic coverage were observed.

Conclusion: We have developed an integrated real-time and high resolution MRCA system optimized for 3T. High SNR and excellent fat suppression were achieved with reasonable susceptibility artifacts. All of the major arteries were imaged in mean scan time of 15 minutes.

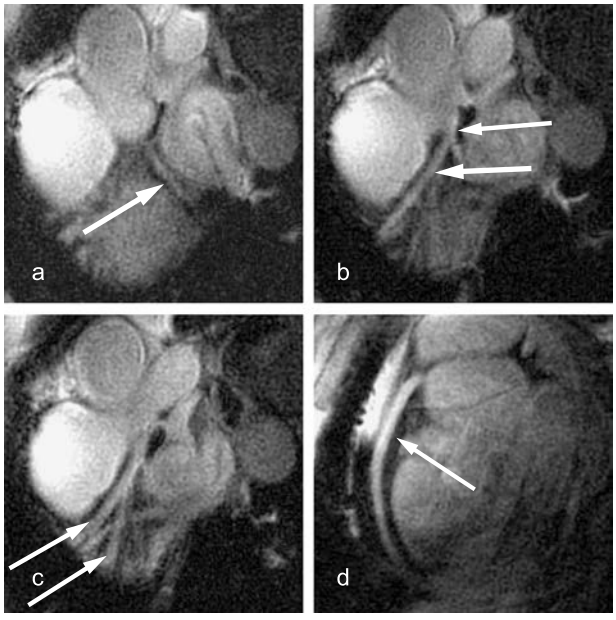

Figure 1.

REFERENCES

Nayak, K., et al. (2003). *11th ISMRM Late-Breaking MR.*
Santos, J., et al. (2002). *Proc. 10th ISMRM*. 686.
Zur, Y. (2000). *Magn. Reson. Med.* 43:410.

218. A Statistical Motion Atlas for Dynamically Assessing Myocardial Function in MRI

Caroline Petitjean, PhD,[1] Nicolas F. Rougon, PhD,[1] Philippe Cluzel, PhD, MD,[2] Françoise Prêteux, PhD,[1] Philippe Grenier, MD.[2] [1]*ARTEMIS Project Unit, GET/INT, Evry, France,* [2]*Service de Radiologie, Groupe Hospitalier Pitié-Salpêtrière, Paris, France.*

Introduction: Tagged MRI provides a noninvasive way to assess the regional function of the heart. We have recently proposed a reliable and unsupervised method for dynamically quantifying myocardial strain from MR images. We here describe how this technique allows to create a numerical motion model for the human normal heart, enabling a model-oriented approach for myocardial strain measurement.

Purpose: To build a statistical motion atlas for the human healthy heart to be used for quantitatively assessing myocardial contraction from tagged and cine MR sequences.

Methods: A database comprising 20 jointly acquired tagged and cine MR cardiac exams of healthy subjects was built. MR sequences comprising 12 short- and 8 long-axis views were acquired during multiple breath holds on a 1.5T GE scanner (1.48 mm in-plane resolution, 45 ms time interval, 17–27 phases per cardiac cycle, SPAMM tagging grid, 10 mm tag spacing).

Atlas construction and manipulation both rely on a non rigid registration (NRR) technique based on generalized information measures. It allows to perform motion estimation and anatomical alignment in an accurate, segmentation-free and unsupervised way, by maximizing the statistical similarity of proton density distributions of image pairs. Atlas construction—The motion atlas is built from a training data set according to a three-step scheme: 1) *intra-subject motion estimates* are derived from tagged sequences by *non parametric* NRR of each phase onto the end-diastolic frame; 2) *inter-subject anatomical alignment* is performed from cine data by NRR of a designated end-diastolic reference image onto end-diastolic subject frames; subject motion data are then warped by the corresponding subject-reference transform; 3) *principal component analysis* of aligned motion data is achieved at each slice level and cardiac phase to produce a

Copyright © Marcel Dekker, Inc. All rights reserved.

ORDER REPRINTS

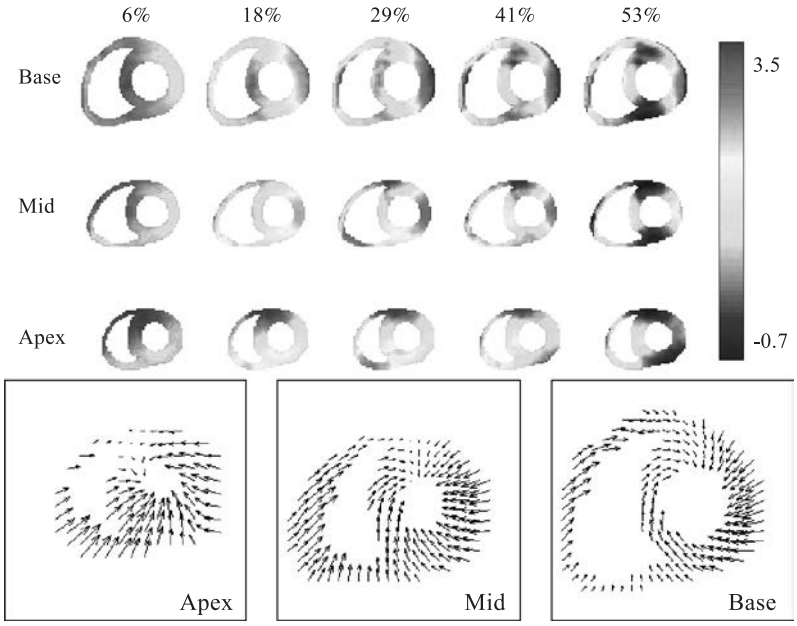

Figure 1.

statistical atlas, comprising a mean motion field and a set of so-called *eigenmotions* encoding kinematic variability. Atlas-based strain assessment—Eigenmotions define a heart-dedicated motion basis. Modeling myocardial displacements as linear combinations of the mean and eigenmotions enables *parametric* motion estimation from arbitrary tagged data. This is achieved in two steps: 1) *atlas alignment onto subject anatomy* is performed from cine end-diastolic images by NRR of the atlas reference onto the subject frame; 2) *atlas-based motion estimation* is achieved by *parametric* NRR of tagged images onto the end-diastolic phase. This yields a compact description of myocardial contraction at every slice level over the whole cardiac cycle. Local and segmental deformation parameters are finally computed from parametric motion data.

Results: A statistical atlas, comprising a mean motion field and 7 eigenmotions per slice and phase, has been generated from a 11 exams training set borrowed from the database, at 3 short-axis and 3 long-axis levels and 17 phases. Eigenmotions retain 95% of motion variability within the training set. Pixel-scale and segmental deformation maps—radial/longitudinal contraction, torsion, strains and shears—have been computed from the mean motion model (shown at 3 short-axis levels at systole). They provide local and regional quantitative reference models of myocardial function over the cardiac cycle (radial contraction during systole is illustrated). Atlas-based motion estimation has then been performed on healthy MR exams outside the training set. The derived parametric motion estimates have been compared to direct measurements via non parametric NRR. Results indicate that parametric estimates differ by less than 1 pixel in magnitude and 4 degrees in orientation from non parametric measurements, while leading to a notable representation compactness gain (7 scalar coefficients instead of 5500 motion vectors per level and phase) (Fig. 1).

Conclusions: Atlas-based NRR allows for automated, fast and reliable motion estimation and quantitative strain analysis over the whole myocardium, while delivering a compact description of myocardial contraction.

219. Electromechanical Modelling of the Myocardium Using XMR Interventional Imaging

Maxime Sermesant,[1] Kawal S. Rhode,[1] Sanjeet Hegde,[1] Gerardo I. Sanchez-Ortiz,[2] Daniel Rueckert,[2] Pier Lambiase,[3] Clifford A. Bucknall,[3] Derek L. G. Hill,[1] Reza Razavi.[1] [1]*Department of Imaging Sciences, King's College London, London, United Kingdom,*[2]*Department of Computing, Imperial College London, London, United Kingdom,* [3]*Department of Cardiology, St Thomas' Hospital, London, United Kingdom.*

Copyright © Marcel Dekker, Inc. All rights reserved.

ORDER REPRINTS

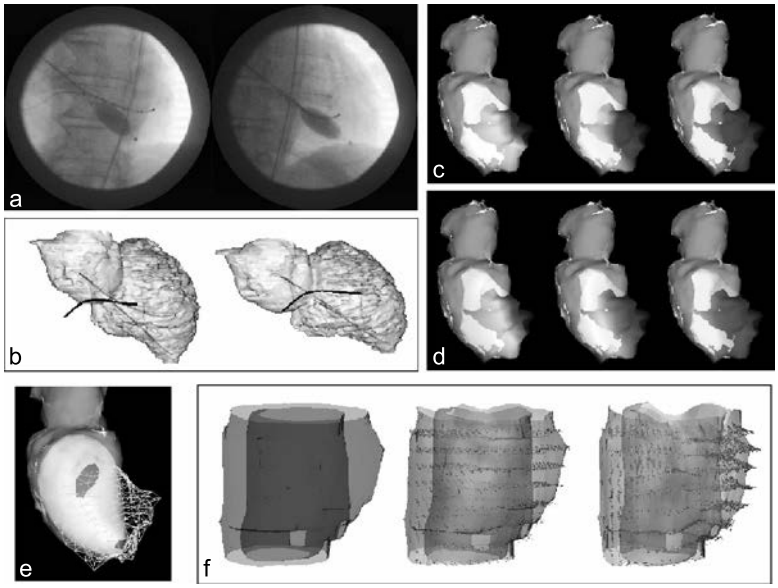

Figure 1. (*View this art in color at www.dekker.com.*)

Introduction and Aim: Myocardial electrophysiology study (EPS) is carried out prior to procedures such as radio frequency ablation or biventricular pacing for heart failure. Under x-ray fluoroscopic guidance, the procedures are often lengthy and there is considerable delivered x-ray dose. Electrophysiological mapping systems such the EnSite system have made some progress to facilitate EPS procedures. We are undertaking a programme of XMR guided EPS procedures using the EnSite system. Cardiac MR imaging can be used to obtain anatomical and functional information prior to and after the procedure. We have previously reported a technique to register MR and x-ray images obtained in the XMR environment. In the current work we apply our technique to EPS procedures with the aim to validate our electromechanical model of the heart. We present the initial results from our first case.

Method: Our XMR facility consists of a Philips Intera I/T 1.5T MR system and a Philips BV Pulsera mobile cardiac x-ray system. The patient (male, age 68) was catheterised under local anaesthetic to assess the optimal location for biventricular pacing. Initially, MR imaging was performed. A volume scan of the heart was acquired using an SSFP sequence (3 phases, 256×256 matrix, 120 slices, resolution $= 1.48 \times 1.48 \times 1.0$ mm, TR $= 3.2$ ms, TE $= 1.6$ ms, flip angle $= 45^{\circ}$) and CSPAMM spiral tagged images were acquired in both short and long axis views (35 phases, 256×256 matrix, 9 slices SA and 5 slices LA, resolution $= 1.76 \times 1.76 \times 12.0$ mm, TR $= 13.0$ ms, TE $= 1.1$ ms, flip angle $= 30^{\circ}$, tag spacing $= 6$ mm). The patient was then transferred to the x-ray system and an EPS was carried out. The EnSite system used a balloon catheter and a roving catheter that were placed in the left ventricle of the patient. The system created a surface model of the chamber and interpolated the measured electrical activity onto this surface. Biplane x-ray images were acquired with the catheters in place and registered to the MR data. The left heart was segmented from MR data. Using the registered x-ray images, the location of the catheters was found in the coordinate system of the segmented MR data. The EnSite surface model was registered to the segmented MR data using the known location of the catheters in these two coordinate systems. It was then deformed to fit the segmented MR data. The tagged MR images were analysed using a non-rigid registration technique to quantify the myocardial motion. Therefore, we were able to combine the anatomical, electrophysiological, and motion data in the same coordinate system. Having achieved this, the measured electrical data were used to initialise our electrophysiological model of the myocardium to generate a simulation of electrical depolarisation based on the reaction-diffusion equations of FitzHugh-Nagumo.

Results: Figure 1a shows the biplane x-ray images. Figure 1b shows the reconstructed position of the catheters within the segmented MR anatomy. Figure 1c shows the EnSite surface model registered to the MR anatomy with the progression of depolarisation for

Copyright © Marcel Dekker, Inc. All rights reserved.

ORDER REPRINTS

three cardiac phases. Figure 1d shows the simulated electrical depolarisation for the same three phases. Figure 1e shows the EnSite surface deformed to fit the segmented MR data. Finally, Figure 1f shows the myocardial deformation computed from the tagged MR data for three phases.

Conclusions: We have proposed a method to integrate anatomical, electrophysiological, and myocardial motion data for patients undergoing EPS. We have presented our initial simulation results for myocardial depolarisation. We are currently applying our electromechanical coupling model to this data to simulate the myocardial contraction and compare this to the measured motion from the tagged MR images. Our registration technique will aid in EPS procedure guidance, and using our electromechanical model we will be able to simulate the outcome of different pacing strategies.

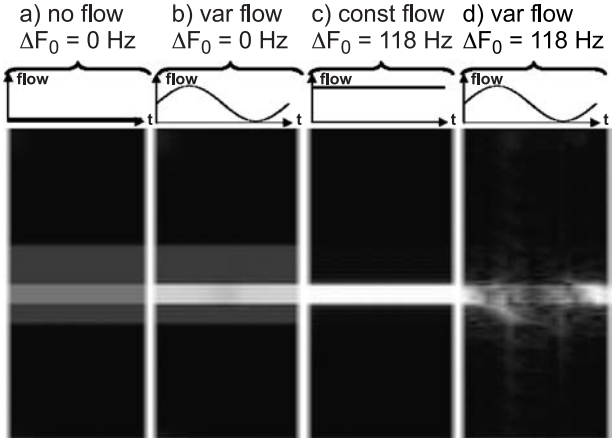

Figure 2. Simulations for different flow patterns and different frequency offsets. The constant (const) flow and the maximum of the sinusoidal (var) flow were both 50 cm/s. The frequency offset of 118 Hz corresponds to a location close to a dark band (0.5/TR = 132 Hz). Simulations show the through-plane flow transient artifact only in case of variable flow and frequency offset. Contrast was cut in half for c) and d) compared to a) and b) as the maximum signal intensity was more than doubled.

220. Understanding Flow Artifacts and Localized Frequency Determination in Cardiac SSFP Imaging

Michael Schär, Sebastian Kozerke, Peter Boesiger. *Institute for Biomedical Engineering, University and ETH Zurich, Zurich, Switzerland.*

Introduction: Balanced steady state free precession (SSFP) techniques offer excellent contrast between myocardium and blood at a high signal-to-noise ratio. At 1.5T, SSFP imaging has become the method of choice for the assessment of cardiac function. Recently it has been reported that frequency offsets due to either wrong resonance frequency determination (F_0) or field inhomogeneity cause flow related artifacts in SSFP imaging (Li, 2003; Markl, 2003). This prompts for an improved shimming and F_0 determination procedure for SSFP imaging, in particular at 3.0T given the larger field inhomogeneities at the higher field strength.

Purpose: To understand flow and resonance frequency dependent artifacts in SSFP imaging and to develop a shimming and F_0 determination method for artifact free SSFP imaging.

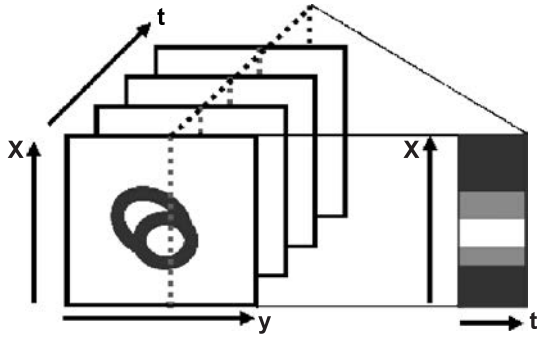

Figure 1. The simulations are performed for one line of a short axis view image along phase-encode direction (x) for 20 heart phases within the cardiac cycle.

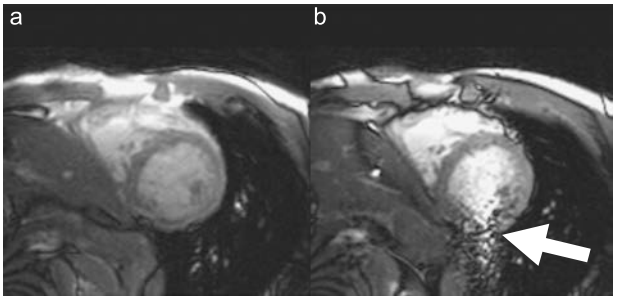

Figure 3. a) Short axis SSFP function time-frame at early diastole measured with localized 2nd order shimming and optimal F_0 as calculated with the proposed method. b) The same acquisition as in a) with a frequency offset of 100 Hz causing a through-plane flow transient artifact (white arrow).

Copyright © Marcel Dekker, Inc. All rights reserved.

ORDER REPRINTS

Methods: Simulations incorporating field inhomogeneity, variable flow, ''out-of-slice'' contribution and phase encoding for spatial localization were performed on a PC using MATLAB (MATLAB, Natick, MA). Longitudinal and transversal magnetization were calculated using the numerical solutions of the Bloch equations for a SSFP cine acquisition. The magnetization matrix incorporated static cardiac muscle and flowing blood including an ''out-of-slice'' segment which was not affected by the excitation radio-frequency pulses. Image profiles along the x direction with 128 phase-encode steps were reconstructed using the Fast Fourier transform. Three different flow patterns were simulated: no flow, constant flow of 50 cm/s, and sinusoidal flow. The following parameters were used: flip angle=40°, TR=3.8 ms, FOV=320 mm, heart rate=60 bpm, 20 cardiac phases, $T1_{blood}$=1512 ms, $T1_{muscle}$=1115 ms, $T2_{blood}$=141 ms, $T2_{muscle}$=41 ms.

For localized 2nd order shimming (Schär, 2003) and F_0 determination, a software tool was implemented on a PC. The shim procedure is based on a measured field (B_0)-map. The calculated shim corrections are then added to the measured B_0-map and used to calculate the optimal F_0 at the ''phase center'' of the shimmed region of interest.

SSFP short axis views were acquired on a 3.0T Intera whole body MR system (Philips Medical Systems, Best, The Netherlands) using the same parameters as for the simulation.

Results: Only one line of a short axis image was simulated in phase encoding direction (Figure 1). The second dimension in the figures was used as the time dimension with 20 heart phases.

Figure 2 shows the results of the simulation. Inflow into the slice increases the signal as a function of flow velocity (Figure 2b). A frequency offset close to a dark band significantly increases the signal intensity of the flowing blood (Figure 2c) as has been shown by Markl (2003). In addition, frequency offset and variable flow can lead to severe artifacts (Figure 2d) along the phase-encode direction if large flow variations are present.

This through-plane flow transient artifact is also seen in-vivo if the resonance frequency is not properly determined. In Figure 3, a single time-frame during flow deceleration of a cine short-axis SSFP acquisition obtained with localized 2nd shimming is shown for (a) an acquisition at optimal F_0 and (b) an acquisition at a frequency offset of 100 Hz.

Discussion: In this work it is shown that through-plane flow transient artifacts emerge at locations close to dark band artifacts if there is through-plane flow of variable velocity. Spins flowing into the imaging plane at the position of a dark band will generate magnetization of high variance in phase and magnitude as they are still in a transient phase and will, therefore, cause false phase encoding.

Using localized shimming and F_0 determination, flow-related artifacts are efficiently reduced facilitating artifact-free cine SSFP imaging at 3.0T.

REFERENCES

Li, W. (2003). *Proc. ISMRM*. 1568
Markl, M. (2003). *Proc. ISMRM*. 293
Schär, M. (2003). *Proc. ISMRM*. 174.

Copyright © Marcel Dekker, Inc. All rights reserved.

Marcel Dekker, Inc.
270 Madison Avenue, New York, New York 10016

Request Permission or Order Reprints Instantly!

Interested in copying and sharing this article? In most cases, U.S. Copyright Law requires that you get permission from the article's rightsholder before using copyrighted content.

All information and materials found in this article, including but not limited to text, trademarks, patents, logos, graphics and images (the "Materials"), are the copyrighted works and other forms of intellectual property of Marcel Dekker, Inc., or its licensors. All rights not expressly granted are reserved.

Get permission to lawfully reproduce and distribute the Materials or order reprints quickly and painlessly. Simply click on the "Request Permission/ Order Reprints" link below and follow the instructions. Visit the U.S. Copyright Office for information on Fair Use limitations of U.S. copyright law. Please refer to The Association of American Publishers' (AAP) website for guidelines on Fair Use in the Classroom.

The Materials are for your personal use only and cannot be reformatted, reposted, resold or distributed by electronic means or otherwise without permission from Marcel Dekker, Inc. Marcel Dekker, Inc. grants you the limited right to display the Materials only on your personal computer or personal wireless device, and to copy and download single copies of such Materials provided that any copyright, trademark or other notice appearing on such Materials is also retained by, displayed, copied or downloaded as part of the Materials and is not removed or obscured, and provided you do not edit, modify, alter or enhance the Materials. Please refer to our Website User Agreement for more details.

Request Permission/Order Reprints

Reprints of this article can also be ordered at

http://www.dekker.com/servlet/product/DOI/101081JCMR120028312